2022-010

Multidimensional Optimizations of Photon Flux by Alignment of the H.E.S.S. Astro Quantum Optics Setup

Master's Thesis in Physics

Presented by
Frederik Wohlleben
22.07.2022

Erlangen Centre for Astroparticle Physics

Friedrich-Alexander-Universität Erlangen-Nürnberg

Supervisor: Prof. Dr. Stefan Funk
Co-Supervisor: Prof. Dr. Gisela Anton

Abstract

The Astro Quantum Optics group at the Erlangen Centre for Astroparticle Physics aims to measure the angular diameter of stars. This is done by using intensity interferometry on the H.E.S.S. telescopes in Namibia. This work covers the procedure of finding the spot of the telescope and guiding the light beam of the telescope into the optics of the measurement setup. It explains how a multidimensional optimization of the positions of different optical elements can be performed, using the measured photon rate as the measure for optimization. Additionally it gives an overview over which techniques worked in the lab and on the telescope.

Index

Chapter I

Measuring small Angular Diameters

1.1 Motivation

"Measure what can be measured,
and make measurable what cannot be measured."

- Galileo Galilei

As physics aims to find mathematical laws for natural phenomena, measurement processes have always been and will always be crucial for the formulation or confirmation of any physical theory. Therefore, they are a substantial part of any experimental physicist's work and not to be underestimated in their impact. In fact new methods of measurement which where first implemented by physicists have finally found widespread adoption in various other parts of science, technology and society. Be it precise time measurements which now allow everyone to find their position on earth in a matter of seconds via GPS or small-scale spatial measurements, as performed by scanning electron microscopes which enable new research in biology and medicine. Taking this perspective it is no surprise that experimentalists from around the world are constantly trying to use new technologies as well as established mathematical theories in their endeavor for ever more precise ways of measuring.
The Astro Quantum Optic (AQO) group at Erlangen Centre for Astroparticle Physics (ECAP) aims to precisely measure the angular diameter of stars as a first step in a search for a high angular resolution imaging system in the visible spectrum. The following sections will give a brief overview of the possible methods of achieving high angular resolutions as well as their limitations.

1.1.1 Observations in the Optical Spectrum with(out) Classical Telescopes

The simplest way to make observations of the sky is using the human eye. It offers an angular resolution of $\approx 1'$ [1], [1, p. 358]. From experience, one knows that if one looks at astronomical objects, this resolution is sufficient to 'measure' the angular diameter of the sun ($31'\,27''$ to $32'\,31''$ [2]) [2] and the moon ($\approx 31'\,36''$) [3]. Even though some people might believe to be able to resolve the size of stars and planets with their eyes as well, what they actually perceive is usually a point-like source which seems to be extended due to an interplay of the object's brightness and atmospheric turbulence. For reference: the largest (as seen from earth) of these objects (Jupiter) has an angular diameter of just $30'\,30''$ to $50'\,6''$ [4] and is therefore already slightly below the human eye's resolution.
To increase the resolving power of the human eye, simple optical telescopes were constructed and used for astronomy from Galileo Galilei's time on. The angular resolution of an ideal optical telescope α_{min} is limited by the diffraction of light. In the wave picture, light behaves as a wave and is diffracted when it passes through an aperture. According to the Rayleigh criterion, two point sources can only be differentiated from each other if the maximum of the diffraction pattern of one source is at least in the first minimum of the second source (or even further away), resulting in the following equation [1, pp. 356-368]

$$\alpha_{\text{min}} = \arcsin\left(1.22 \cdot \frac{\lambda}{D}\right) \approx 1.22 \cdot \frac{\lambda}{D} \tag{1.1}$$

where λ is the wavelength and D the aperture of the optical telescope. For example, a typical amateur telsecope with an aperture of $D = 200\,\text{mm}$ offers an angular resolution of $0.63''$ at a wavelength of $500\,\text{nm}$, which is sufficient for resolving Jupiter with a good degree of detail. Meanwhile, state of the art observatories, such as the Gran Telescopio Canarias of the Keck I + II telescopes, feature apertures of up to $10\,\text{m}$, pushing the theoretical resolving power to $12.6\,\text{mas}$[3]. However, extending the aperture ever further, is usually not a feasible way due to disproportionally increasing complexity and cost. Further, the earths atmosphere limits the resolution that can be achieved. This so called 'seeing' is location dependent but can usually be approximated as $\approx 3''$. For this reason physicists came up with a new way.

[1] An arcminute is $\frac{1}{60}$ th of a degree. It will be abbreviated as ' for the rest of this thesis.
[2] An arcsecond is $\frac{1}{60}$ th of an arcminute. It will be abbreviated as '' for the rest of this thesis.
[3] A milliarcsecond is $\frac{1}{1000}$ th of an arcsecond. It will be abbreviated as 'mas' for the rest of this thesis

1.1.2 Amplitude Interferometry

Amplitude interferometry surpasses the limits of diffraction by using multiple (in the simplest configuration two) telescopes. A typical configuration of such an interferometer can be seen in fig. 1.1a.

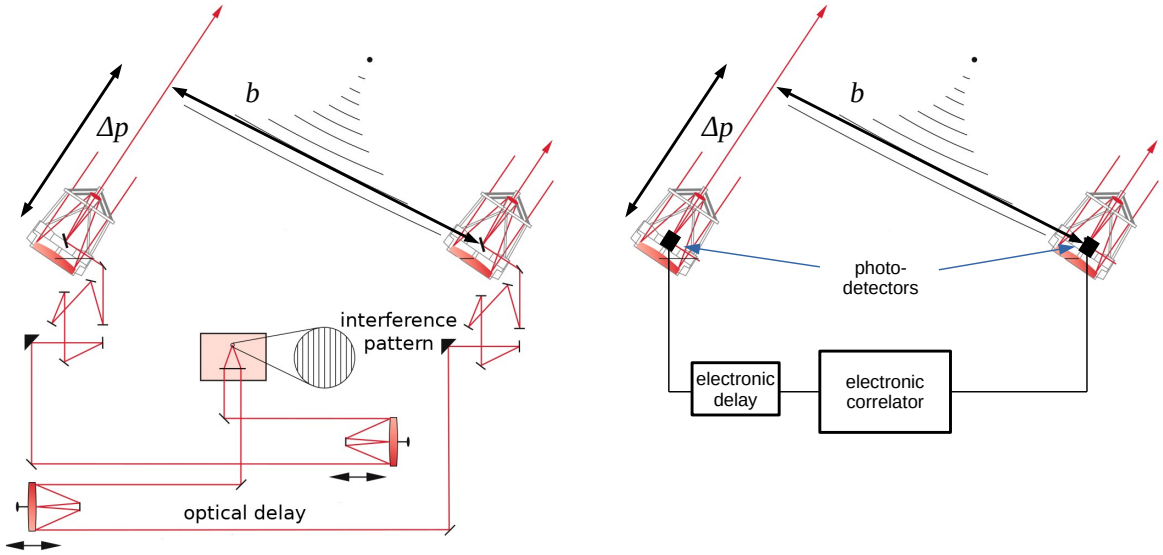

(a) Amplitude interferometry

(b) Intensity interferometry

Figure 1.1: Schematics of different interferometers adapted from [1, p. 225]

In amplitude interferometry one does not increase the size of the telescope, but instead uses two telescopes placed at a projected distance in the plane perpendicular to the direction of the incoming light, called the baseline b. The light is collected in both telescopes (whose size now is merely interesting for the light collection capabilities but not for the resolution [4]) and from there fed through an optical system towards a unit where it is interfered. To preserve the phase of the light, even as the path delay between the two telescopes Δp changes over time (due to the rotation of earth and the resulting change in position of the observed object relative to the telescopes), an optical delay path is added to at least one of the telescopes' light paths. When the light beams from both telescopes are interfered, the resulting fringe pattern allows for a calculation of the angular diameter of the star.
To put the above into equations one can image an amplitude interferometer as a simple double

[4] Actually if the size of the telescopes gets too big the angular resolution of the telescope gets worse. This is due to the fact that the signal from each telescope is less localized and therefore does not display the characteristics at one point but instead at a wider range in space

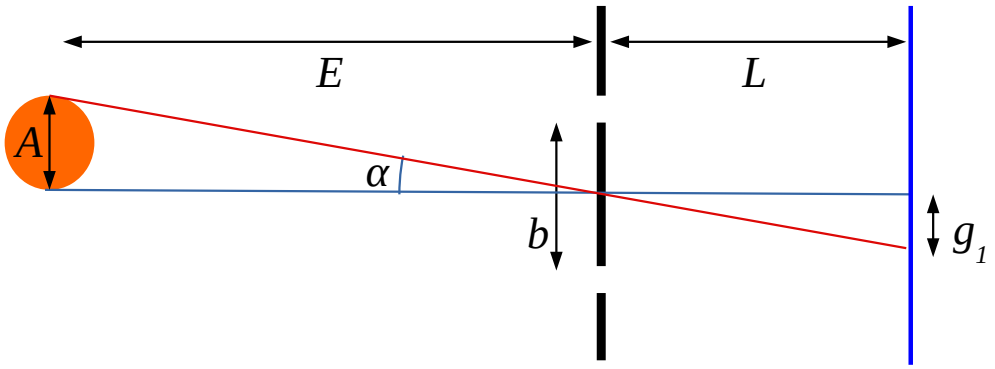

Figure 1.2: Sketch of a stellar amplitude interferometer. E is the distance between the stellar object and the apertures of the telescopes, L is the distance between the screen and the apertures, b is the distance between the centers of the apertures, A the absolute diameter of the stellar object and α the angle between the two rays of light.

slit experiment, with the telescopes as the "slits" and the baseline b as the separation between them. From simple trigonometric considerations developed out of fig. 1.2, one can write

$$\sin\alpha = \frac{g_1}{L} = \frac{\Delta s}{b} \tag{1.2}$$

with the parameters taken from fig. 1.2 except for Δs which is the path length difference between the red and the blue path on the right side of the slits. We know that for constructive interference $\Delta s = n\lambda$ and for destructive interference $\Delta s = \left(n + \frac{1}{2}\right)\lambda$ with $n \in \mathbb{N}$ holds. This is true for a point like source in the far field (we can assume plane waves at the double slit). As we are looking at an extended source, we get a slightly different behavior: One can imagine an extended source as a large number of point sources, each one with its own fringe pattern. All of these fringe patterns overlap and add up to a pattern, which can be quite complicated. Therefore, one is only interested in the special case, where the outermost points of the star are exactly "out of sync", meaning that the maxima of the first fall into the minima of the second fringe pattern. Here the pattern vanishes. This is the case if $\Delta s = \frac{1}{2}\lambda$. The baseline at which we get a vanishing pattern will be called b_0 from here on. One can therefore use this condition to rewrite the right hand side of eq. (1.2) as

$$g_1 = \frac{\lambda L}{2b_0} \tag{1.3}$$

From fig. 1.2 one can see that

$$\frac{A}{E} = \frac{g_1}{L} \tag{1.4}$$

as the triangles are similar. Putting eq. (1.2), eq. (1.3) and eq. (1.4) together, we can write

$$\frac{A}{E} = \frac{g_1}{L} = \frac{\left(\frac{\lambda L}{2b_0}\right)}{L} = \frac{\lambda}{2b_0} = \sin\alpha \tag{1.5}$$

which can be rewritten as

$$\alpha = \sin^{-1}\left(\frac{\lambda}{2b_0}\right) \approx \frac{\lambda}{2b_0} \tag{1.6}$$

This leaves the astronomer with one simple equation to calculate the angular diameter α of a star from the baseline b_0. Comparing this to eq. (1.1), we can easily see that we get a similar resolution limit as in the case with the optical telescope, but now it is the baseline b_0 that limits the resolution and not the aperture D of the actual telescope, which is a huge improvement.
Amplitude interferometers were first built in the 1920s at the Mount Wilson Observatory [5] by Albert Michelson and Francis Pease. Their instrument had a baseline of 20 feet (≈ 6.1 m) and thereby already allowed for a measurement of Betelgeuse's angular diameter, which was found to be 47 mas [5] [6]. Even thought such an amplitude interferometer is already a huge improvement from a normal telescope in terms of angular resolution, it faces two major challenges:

- Disturbances in earth's atmosphere tend to shift the phase of light. As the disturbances are quite local, they are already noticeable for smaller baselines but make larger baselines unfeasible.
- The precision of the system - especially of the optical delay - has to be smaller than the wavelength of the incoming light. As visible light is in the hundreds of nanometer range, the required precision is really high, which makes it hard to realize larger baselines and even makes small baselines quite expensive.

For these reasons another way of measuring even smaller angular diameters in the visible spectrum was developed [5].

1.1.3 Intensity Interferometry

Intensity interferometers (compare fig. 1.1b) might look like a minor change to the setup, but the physical description is fundamentially different. Due to this complexity, only a rough setup

[5] While the above is true for optical light, it is not for other parts of the electromagnetic spectrum. Especially in radio-astronomy where one can actually record the whole incoming wave with a somewhat decent sampling-device and later on digitally "interfere" it with waves from other locations and wavelengths (and therefore tolerances) are in the mm regime or above, it is quite a potent tool as the Event Horizon Telescope keeps showing.[7]

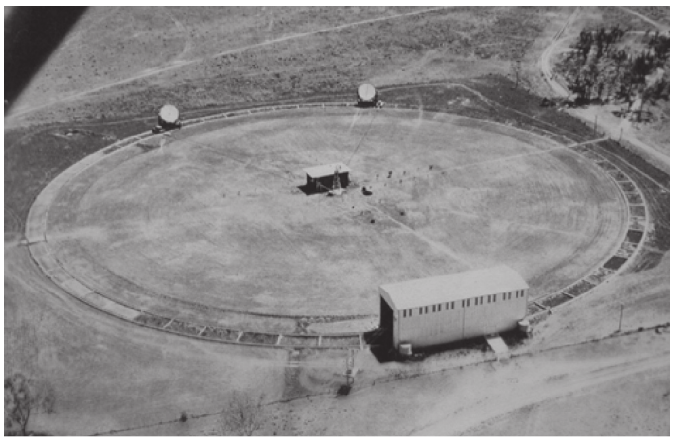

Figure 1.3: Aerial view of the Narrabri Stellar Intensity Interferometer, taken from [9]

is described here, while section 1.2 will feature a more detailed description of the physics.
To get around the problems of amplitude interferometry, Hanbury Brown and Twiss came up with a modified and a relatively simpler setup (compare fig. 1.1b). Instead of redirecting the light collected by the two telescope through an optical system, they used photomultiplier tubes (PMTs) to measure the light in both telescopes. The resulting (now electrical, not optical) signals then pass through several components, including a variable time-delay before being correlated.
Even thought using electrical signals instead of the light itself might seem like a minor change, it is not. When the light itself is used for interference, its wavelike nature (frequency and especially phase) is exploited, while with the photo-detectors one sees single photons and therefore gets into the field of quantum optics. That is the difference on the physics side. From the engineering perspective, the electronic nature of the signal now simplifies the experiment. No optical path delay is needed anymore, as cables and electronics are used for this purpose. This enabled Hanbury Brown and Twiss to put their telescopes on railroad tracks to achieve a plethora of different baselines and orientations. An additional advantage of this method is that these electronic signals can (nowadays) be stored, duplicated and replayed without significant losses. This is especially interesting for larger baselines and setups of more than two telescopes with multiple baselines. After demonstrating the capabilities of their technique in 1956 by measuring Sirius ($6.8\,$mas) in England, Hanbury Brown and Twiss moved on to build the Narrabri Stellar Intensity Interferometer (NSII) (compare fig. 1.3) in Australia which allowed for further research and the measurement of objects as small as $0.42\,$mas (ζ Pup) [8].
In 1974, the NSII was decommissioned and since then no significant measurements have been done in the field of optical astronomical intensity interferometry.
Only in the last few years this method has gained some traction, as suitable telescopes were built for another reason.

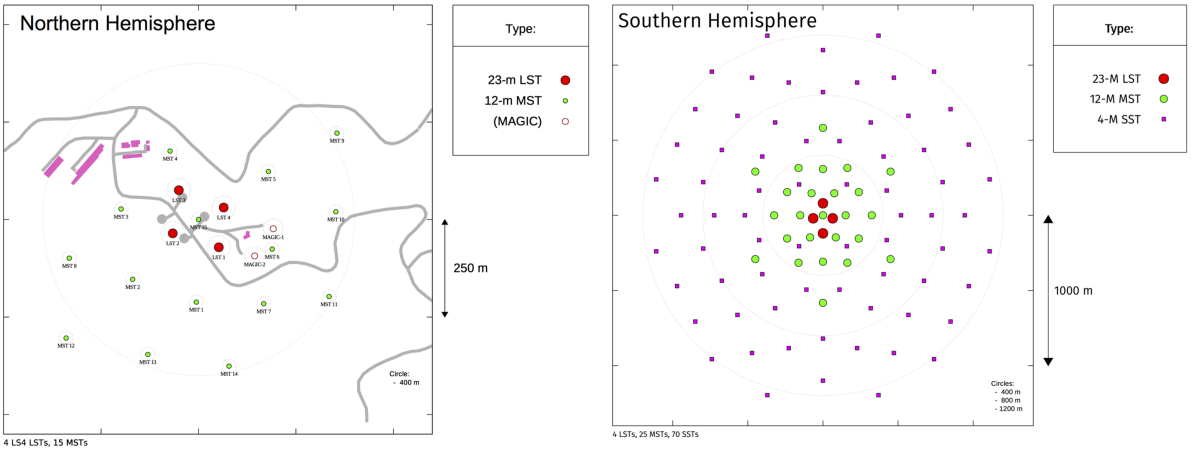

Figure 1.4: Map of the planned CTA Telescope-Arrays, taken from [9]. One can clearly see how many baselines would be possible with the large number of telescopes.

Intensity Interferometry at IACTs: In the early 2000s, multiple arrays of Imaging Atmospheric Cherenkov Telescopes (IACTs) were constructed around the globe to measure very high energy gamma rays. Each IACT consists of a set of mirrors with a total diameter of typically about 10 or more meters. These IACTs are usually arranged in arrays to benefit from coincidence measurements. As they cannot be used for their intended purpose during times of bright moonlight, they sit idle for about a third of the night time, potentially allowing for intensity interferometry measurements to be conducted during this time. For this reason, there is currently research going on at the VERITAS, MAGIC and HESS telescopes on how to efficiently implement intensity interferometry in IACTs with the aim to make this a default feature of the upcoming Cherenkov Telescope Array (CTA).
As CTA will have two sites, one on the canary islands and one in Chile, it offers sky coverage of both northern and southern hemisphere. Due to the layout of the array (compare fig. 1.4) it will be possible to measure many baselines at the same time, allowing for observations of events that happen at much shorter timescales. Additionally one can choose baselines at different orientations relative to each other allowing to even got into two-dimensional imaging, which would further increase the capabilities of an intensity interferometer installed on CTA.

1.2 Physical and Mathematical Background

To gain a deeper understanding of the physics of these types of interference experiments one needs to have a look at the mathematical foundations behind light and its propagation. This section gives a short overview over the major concepts and tries to make the connection between the classical and the quantum optical worlds.

1.2.1 Classical Optics

Coherence and the $g^{(1)}$ function

The concept of coherence originates from classical wave optics. It can generally be understood as a measure for the 'stability' of light or rather an electromagnetic field E. For an intuitive understanding of coherence, one could ask whether the light at two points in space-time $(t_1, \vec{r_1})$ and $(t_2, \vec{r_2})$ in a field would lead to a stable interference pattern.
To mathematically quantify the coherence of light, the $g^{(1)}$ function is used

$$g^{(1)}(\vec{r}_1, \vec{r}_2, t, \tau) = \frac{\langle E^*(\vec{r}_1, t) \cdot E(\vec{r}_2, t+\tau)\rangle}{\sqrt{\langle E^*(\vec{r}_1, t) E(\vec{r}_1, t)\rangle \langle E^*(\vec{r}_2, t+\tau) E(\vec{r}_2, t+\tau)\rangle}} \tag{1.7}$$

where the * denotes the complex conjugate and $\langle \cdots \rangle$ the timely average. Mathematically, it is interesting to notice that in the numerator the complex nature of the electric fields is used, which contains information about both the amplitude and the phase. Therefore, this obviously is a concept of classical wave optics. The denominator is just a simple normalization. Important values of $g^{(1)} = 1$ for fully coherent light and $g^{(1)} = 0$ for completely incoherent light.
Usually one does not change both the points in space and time but instead differentiates between temporal coherence and spatial coherence by changing only the respective parameter. It is important to note, that a local change in the direction of the light's propagation is regarded the same as a change in time, leaving only two dimensions for the spatial coherence.
To give some practical examples: A monochromatic source will display perfect temporal coherence as the wavelength of the emitted light does not change, while a plane wave (e.g. from a point source at an infinite distance) would display perfect spatial coherence. The spatial coherence can therefore be used as a measure of the wave's propagation through space from its origin, while the temporal coherence is used to describe the temporal stability of the wave respectively its production process. This makes coherence interesting for physicists, as the coherence of light usually contains a lot of information about its source.

Van Cittert-Zernike Theorem

As stated before, one can extract information about the source from the measured spatial coherence $g^{(1)}(\vec{r_1}, \vec{r_2})$. To actually make use of the measured $g^{(1)}$ function, the 'van Cittert-Zernike theorem' is used. In this section an overview over its use is given. One starts with the theorem under the assumption that the observer is in the far field of the observed object (as stated in [10, p. 191]):

$$g^{(1)}(\vec{r}_1, \vec{r}_2) = e^{ik(\vec{r_2}-\vec{r_1})} \frac{\int_\sigma I(\vec{r}') e^{-ik(\vec{s_2}-\vec{s_1})\cdot\vec{r}'} d^2\vec{r}'}{\int_\sigma I(\vec{r}') d^2\vec{r}'} \tag{1.8}$$

where $I(\vec{r}')$ is the spatial intensity distribution (or to put it simply the 2-dimensional "image") of the source, while σ is the area of the source and $\vec{s_1}$ and $\vec{s_2}$ are the unit vectors of $\vec{r_1}$ respectively $\vec{r_2}$.
As we are in the far field, we can assume that $\vec{r_1} \approx \vec{r_2}$ which results in a negation of the initial exponential term. If we further assume that the source σ is monochromatic, uniform in intensity ($I(\vec{r}') = \text{const}$), radial and of diameter a and we put the origin of our coordinate system into the center-point of the source, eq. (1.8) simplifies to [6]

$$g^{(1)}(\vec{r}_1, \vec{r}_2) = \frac{\int_{|\vec{r}'|\leq a} e^{-ik(\vec{s_2}-\vec{s_1})\cdot\vec{r}'} d^2\vec{r}'}{\int_{|\vec{r}'|\leq a} \vec{r}' d^2} \tag{1.9}$$

Evaluating this integral in radial coordinates leads to an integral which is the same as in the derivation of Frauenhofer diffraction of a circular aperture. We can therefore rewrite it as

$$g^{(1)}(\vec{r}_1, \vec{r}_2) = \frac{2J_1(v)}{v} \tag{1.10}$$

with $J_1(v)$ the Bessel function of first kind and order and

$$v = \bar{k}\left(\frac{a}{r}\right) b \propto \alpha \cdot b \tag{1.11}$$

where the factor $\bar{k} = \frac{1\pi}{\lambda}$, b is the baseline of our telescopes assuming the telescopes are in the same plane perpendicular to the propagation of light and $\alpha \approx \frac{a}{r}$ the angular diameter of the star in the small angle approximation. One can calculate that $g^{(1)} = 0$ for a baseline

$$b = 0.16\frac{\lambda}{\alpha} \tag{1.12}$$

Therefore, one can now calculate α, by simply varying the baseline and looking at which baseline one gets complete incoherence. A visualization of this can be achieved by plotting $g^{(1)}$

[6] All these assumptions are reasonable and necessary to develop a working amplitude interferometer in the optical spectrum. For radio astronomy the math is not simplified as easily due to the increased wavelengths.

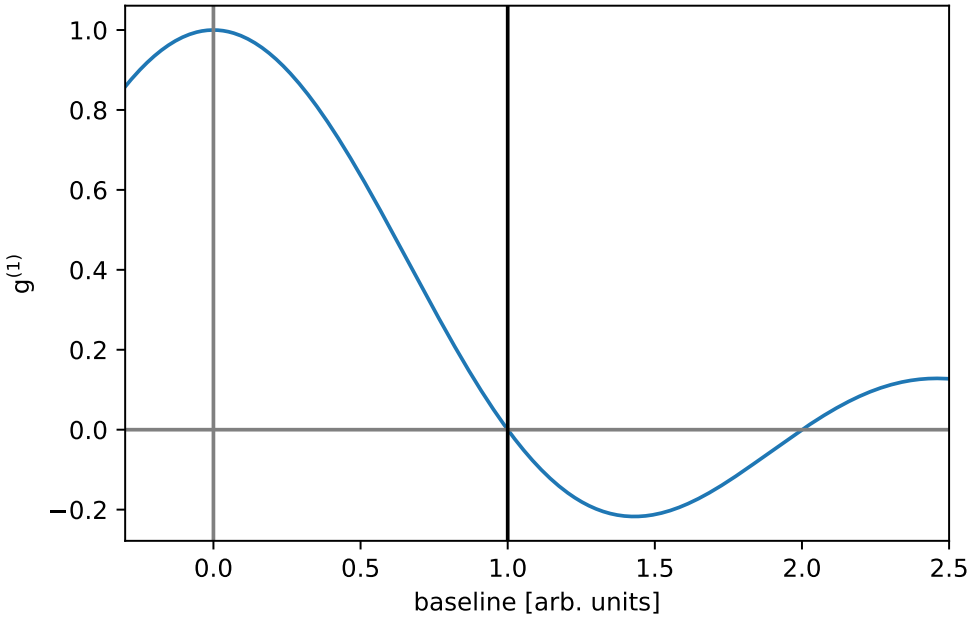

Figure 1.5: Plot of the $g^{(1)}$ function over b. The position of the black vertical line marks the position of the first minimum of the $g^{(1)}$ function which is the baseline where complete incoherence is achieved.

over b (compare fig. 1.5)
Having a closer look at eq. (1.12), one must furthermore conclude that larger baselines are needed for smaller angular diameters.

1.2.2 Quantum Optics

In Quantum Optics, the terms phase and amplitude have no meaning when looking at individual photons. Here one has to define new properties of light. The following section will largely be based on [5].

Rate and Intensity

While in wave optics one normally looks at the amplitude of a wave, this is not a possible measure in quantum optics, as individual photons have no amplitude but instead a specific energy. In quantum optics, a common measure is the rate given in [Hz] which is just a simple count of photons per time.

Intensity is defined as energy per time per area and commonly given in units of $\frac{\mathrm{W}}{\mathrm{m}^2}$. It could therefore be obtained by adding up the individual energies of photons and dividing by the area and time in which the observation took place.
While the name 'intensity interferometry' suggests, that the intensity is the important quantity, in these experiments this is not the case. Coincidentally, when using monochromatic light in most experiments, the energy is of lesser concern and as individual photons are counted, one should rather speak of 'rate interferometry'[7]. Theoretically, the terms 'intensity' and 'rate' could be used interchangeably in intensity interferometry, as for monochromatic light these two are proportional to each other. The main difference in the use of these terms is that when 'rate' is concerned, one usually wants to quantify the average amount of light that is fed into the interferometer over a certain time while 'intensity' commonly describes a function of time where the timely distribution of the individual photons is of interest. This timely function $I(t)$ (not to be confused with the spatial intensity distribution from the previous section) becomes quite important when talking about bunching.

The $g^{(2)}$ function and Bunching

In quantum optics, both phase and amplitude cannot be measured. Instead, one only measures a stream of individual photons giving the intensity $I(t)$. Therefore, seemingly all information about the phase is lost.
This can also be expressed on a mathematical level as the intensity is defined as

$$I(t) = |E(t)|^2 \tag{1.13}$$

where $E(t)$ is the complex electrical field. One easily notices, that the complex phase of the field perishes due to the the square of the absolute value. This makes it obvious that it is not possible anymore to measure the $g^{(1)}$ function (compare eq. (1.7)), as it requires the complete information from both electric fields. Hence, one has to resort to another measure to compare the signals from the two telescopes of the interferometer, namely the $g^{(2)}$ function. It is defined as

$$g^{(2)}(\vec{r_1}, \vec{r_2}, \tau) = \frac{\langle I(\vec{r_1}, t) \cdot I(\vec{r_2}, t+\tau) \rangle}{\langle I(\vec{r_1}, t) \rangle \langle I(\vec{r_2}, t) \rangle} \tag{1.14}$$

where $I(\vec{r}, t)$ denotes the measured intensity at the telescope's location $\vec{r}$ at time t. This quantity can easily be measured, either by the use of electronics or by digital sampling of the

[7] When complaining about the name, one should also mention that technically the light is not interfered either, since interfermoetry is a concept from classical optics. If one wants to be precise the name 'rate correlation' would deliver a better description of the actual method. The term 'intensity interferometry' should therefore rather been understood as an historic artifact from the development of intensity interferometry out of amplitude interferometry, than a physical description of the conducted science.

signal and later processing.
One can rewrite $I(\vec{r},t)$ as

$$I(\vec{r},t) = \langle I(\vec{r})\rangle + \Delta I(\vec{r},t) \tag{1.15}$$

where $\langle I(\vec{r})\rangle$ is the average of $I(\vec{r},t)$ over time and $\Delta I(\vec{r},t)$ contains the deviation from this average at each moment t. Inserting this expression into eq. (1.14) we find

$$g^{(2)}(\vec{r_1},\vec{r_2},\tau) = \frac{\langle(\langle I(\vec{r_1})\rangle + \Delta I(\vec{r_1},t))\cdot(\langle I(\vec{r_2})\rangle + \Delta I(\vec{r_2},t+\tau))\rangle}{\langle\langle I(\vec{r_1})\rangle + \Delta I(\vec{r_1},t)\rangle\cdot\langle\langle I(\vec{r_2})\rangle + \Delta I(\vec{r_2},t)\rangle} = \tag{1.16}$$

as the time average of all the $\langle\Delta I(\vec{r},t)\rangle = 0$. Further, the denominator can be rewritten and the numerator expanded

$$= \frac{\langle\langle I(\vec{r_1})\rangle\cdot\langle I(\vec{r_2})\rangle\rangle + \langle\langle I(\vec{r_1})\rangle\cdot\Delta I(\vec{r_2},t+\tau)\rangle + \langle\Delta I(\vec{r_1},t)\cdot\langle I(\vec{r_2})\rangle\rangle + \langle\Delta I(\vec{r_1},t)\cdot\Delta I(\vec{r_2},t+\tau)\rangle}{\langle\langle I(\vec{r_1})\rangle\cdot\langle I(\vec{r_2})\rangle\rangle} \tag{1.17}$$

which can be simplified to

$$= 1 + \frac{\langle\Delta I(\vec{r_1},t)\rangle}{\langle I(\vec{r_1})\rangle} + \frac{\langle\Delta I(\vec{r_2},t+\tau)\rangle}{\langle I(\vec{r_2})\rangle} + \frac{\langle\Delta I(\vec{r_1},t)\cdot\Delta I(\vec{r_2},t+\tau)\rangle}{\langle\langle I(\vec{r_1})\rangle\cdot\langle I(\vec{r_2})\rangle\rangle} \tag{1.18}$$

We can now get rid of the second and the third term, as the timely average of the fluctuations is zero by definition

$$g^{(2)}(\vec{r_1},\vec{r_2},\tau) = 1 + \frac{\langle\Delta I(\vec{r_1},t)\cdot\Delta I(\vec{r_2},t+\tau)\rangle}{\langle\langle I(\vec{r_1})\rangle\cdot\langle I(\vec{r_2})\rangle\rangle} \tag{1.19}$$

To gain understanding of this new equation we look at the second term. As a first step, we look at $g^{(2)}(\tau = 0)$. This describes the likelihood of two photons arriving at the same time. Here we distinguish three cases:

- $g^{(2)}(\tau = 0) = 1$ **coherent light** :
  In the case of coherent light, the temporal sequence of photons is random. As the time between the individual photons is randomly distributed, the likelihood of two photons arriving at the same time is the same as for any other arbitrary time. Therefore, one can even conclude that $g^{(2)}(\tau) = 1, \forall\tau$. As known from classical optics, a prototypical source of coherent light would be a monochromatic point source seen from infinite distance

- $g^{(2)}(\tau = 0) > 1$ **bunched light** :
  Bunched light is characterized by 'bunches' of photons that clump together. One therefore has a higher likelihood of detecting photons in both spatial and temporal proximity of each other. Consistently, for small values of τ one expects higher values of $g^{(2)}(\tau)$ and lower

ones as τ increases. A typical source of bunched light is a discharge lamp, which displays a fluctuating intensity. However, it can be generally found that at most places where light is emitted from a broader area containing different individual emitters (molecules, atoms, etc.), a certain degree of bunching can be observed. As the individual emitters are not coordinated, this kind of light is also referred to as 'chaotic'

- $g^{(2)}(\tau = 0) < 1$ **antibunched light** :
  Antibunched light is a special case. In antibunched light the photons are spaced out equally, making it unlikely (in the case of ideal antibunched light even impossible) to find two photons at the same time of arrival. Even though antibunched light can be produced artificially with some effort (e.g. repeated excitation of individual atoms), it is not found in nature. As this behavior of the light cannot be explained by any classical model, its existence is a clear indicator for the quantum nature of light.

A star is not a point source but instead its surface can be described as a large area of emitters. Hence, we expect the star's light to be bunched to a certain degree. We can further assume that the bunching decreases as we increase the baseline of our measurement, as the light is not only bunched in time but also space. In order to measure this, we measure the temporal correlation $g^{(2)}(\tau)$ at different baselines and for all baselines note the value for $g^{(2)}(\tau = 0)$. Plotting these values over the baselines gives us the spatial $g^{(2)}$ function $g^{(2)}(b)$. But what does this interesting quantum behavior of light and the spatial $g^{(2)}$ function tell us about the star's angular diameter? To exploit the bunching effect, we need a way to connect it to our previous approach. This can done by the Siegert-Relation

Siegert-Relation

The Siegert-Relation (only valid for chaotic light sources) [11] provides a relation between the $g^{(1)}$ and the $g^{(2)}$ function.

$$g^{(2)}(\tau, \vec{r_1}, \vec{r_2}) = 1 + |g^{(1)}(\tau, \vec{r_1}, \vec{r_2})|^2 \tag{1.20}$$

Knowing this relation, one can easily use the methods previously used in amplitude interferometry to calculate the angular size of a star by simply measuring its $g^{(2)}$ function instead of the $g^{(1)}$ function (compare fig. 1.6).

This finally allows for a calculation of the star's angular diameter with the data obtained from the (compared to an amplitude interferometer) much simpler intensity interferometer. There are however some limitations of intensity interferometry which are not present in amplitude interferometry: For intensity interferometry, one already needs an educated guess about the shape of the investigated object. For stars this is doable, as one can just assume a circular shape. Amplitude interferometry on the other hand can measure any intensity distribution, as a

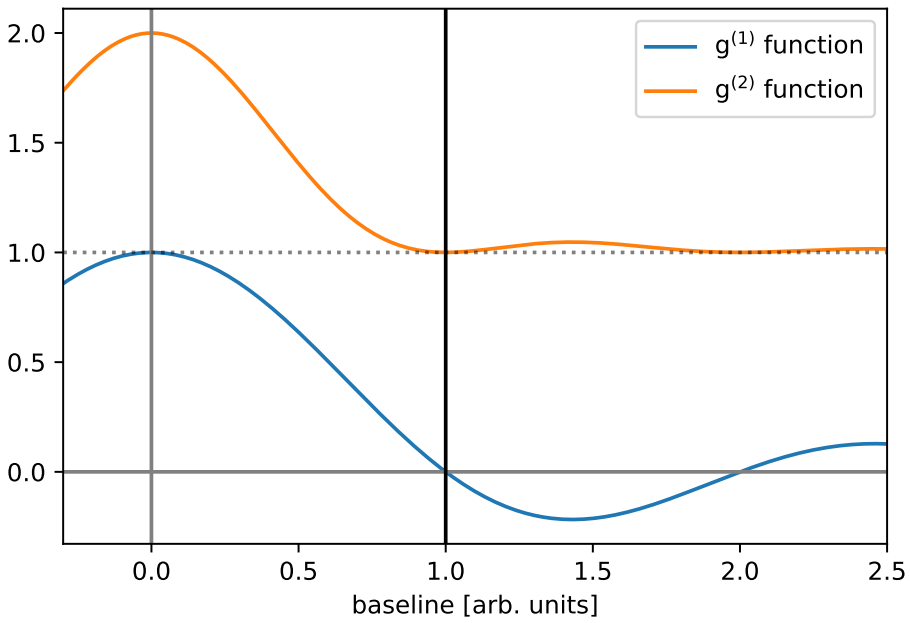

Figure 1.6: Plot of the $g^{(1)}$ and the spatial $g^{(2)}$ function. One can easily see that fitting the $g^{(2)}$ function yields the same results as fitting the $g^{(1)}$ function. The black line marks the baseline at which one would see destructive interference in an amplitude interferometer (compare eq. (1.12)).

Fourier-transform can be used to calculate the actual intensity distribution of the source. Additionally, intensity interferometry suffers from a worse signal to noise ratio which leads to longer measuring times.

Chapter II

Measurement Instruments and Setup

2.1 H.E.S.S. Telescopes

The High Energy Stereoscopic System (H.E.S.S.) is a set of telescopes located in Namibia in the southern hemisphere. It consists of 4 telescopes with a dish diameter of $13\,\mathrm{m}$ (H.E.S.S. phase I), as well as one larger telescope with a larger dish of roughly $28\,\mathrm{m}$ diameter (H.E.S.S. phase II). As for intensity interferometry, one requires at least two (ideally identical) telescopes, only the phase I telescopes are considered in this work.
The H.E.S.S. phase I telescopes were built in the early 2000s and have been operational since 2003 [12]. The following section is largely based on the H.E.S.S. design papers [13] [14] and describes the optical properties of the telescopes.

2.1.1 Mechanics and Layout

The four telescopes are placed in a square with an edge length of $120\,\mathrm{m}$, rotated by $45°$ from north. The combinations of telescopes and the resulting maximal baselines can be found in table 2.1

max. baseline (m)	orientation	telescopes
169.7	North - South	2 & 4
169.7	West - East	1 & 3
120.0	Northeast - Southwest	1 & 4 , 2 & 3
120.0	Northwest - Southeast	1 & 2 , 3 & 4

Table 2.1: Possible maximal baselines with the H.E.S.S. phase I telescopes.

Each telescope consists of a steel structure (compare fig. 2.1) sitting on a concrete foundation. It covers all $360°$ of azimuth range and is able to move from $\approx -35°$ below the horizon to zenith, using a system of servo motors, allowing for a coverage of the entire visible sky. It is important to notice, however, that safe operations are only possible above an altitude of $10°$ above the horizon.

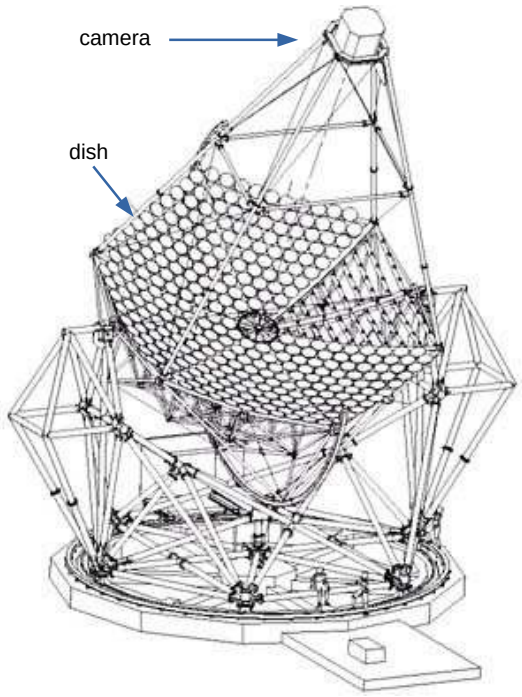

Figure 2.1: Drawing of the H.E.S.S. phase I telescopes' structure. Adopted from [13, p. 4].

The telescope dish (see section 2.1.2) has a diameter of $13\,\mathrm{m}$. The camera sits at the focal point of the dish, which is at a distance of $15\,\mathrm{m}$ from the center of the mirror. It weighs $\approx 900\,\mathrm{kg}$ and is protected by a 'lid' that is closed during daytime and hydraulically opened at night to allow observations. The camera is held in place by a large arm, built from four steel tubes, supported by crossed pairs of steel struts.
As the telescope moves in azimuth and especially in altitude, its structure flexes due to the forces pulling on both the camera and the arm. This leads to a movement, especially of the camera, which has the largest lever arm as seen from the altitude axis. This results in a certain degree of miss-pointing. The miss-pointing of each telescope is recorded in bimonthly calibrations, called 'pointing runs'. The data from these runs is then used to create a pointing model which describes the miss-pointing of each telescope for all possible positions the telescope might be

moved to. A visualization of such a pointing model can be found in fig. 2.2. From the pointing model we can conclude that the deviation of the telescope's pointing is in the order of $5'$. Calculating this back to an absolute value in the focal plane of the telescope, this translates to an absolute misspointing of $\approx 2.2\,\mathrm{cm}$.

2.1.2 Mirrors

As mentioned earlier, the effort and cost of building large mirrors is quite high and grows disproportionately with size. As IACTs do not need 'perfect' mirrors from one piece, the mirrors of the H.E.S.S. phase I telescopes are pieced together from 380 individual circular facets, made from aluminized optical glass.
The facets are arranged in a Davis-Cotton-layout, which is characterized by spherical facets, placed in such a way that they form a large spherical surface. Every facet has a focal length of $15\,\mathrm{m}$, exactly the same as the telescope as a whole. Their specular reflectivity in the range of visible light is at least $80\,\%$.
Each facet has a diameter of $60\,\mathrm{cm}$ and is mounted onto the steel structure at three points, of which two are connected to actuators with a $3\,\mu\mathrm{m}$ positioning step size. This allows the facets to be aligned quite precisely. The reference point for calibration of the facets lies at an altitude of $50°$ above the horizon. Simulations show that as the telescope moves to other altitudes, gravitation leads to misalignment of the facets of up to $0.7'$ for targets close to the horizon.

2.2 Mechanical and Optical Setup for Intensity Interferometry

As described before, the mirrors of the dish focus the light onto its focal point, where the camera is placed. As the camera of the IACTs is designed for other purposes than intensity interferometry, a new sensor needs to be put in place, which is referred to as 'the setup'. It is placed on top of the camera's protective lid, which needs to be closed during the intensity interferometry measurements.

2.2.1 Optical Setup

The purpose of the optical setup is to guide the light coming from the dish, in a way that it can first be filtered by wavelength and then be focused onto a photo detector. The shape of the incoming light for a point-like source is best described by a cone, with its base on the dish and its tip on the focal plane. As the optical plane of the telescope lies approximately on the lid of the camera (on which the setup is mounted), the incoming light is first diverted by $90°$ using a silvered mirror of $254\,\mathrm{mm}$ x $400\,\mathrm{mm}$ (thickness $1\,\mathrm{mm}$) placed at $45°$ relative to the

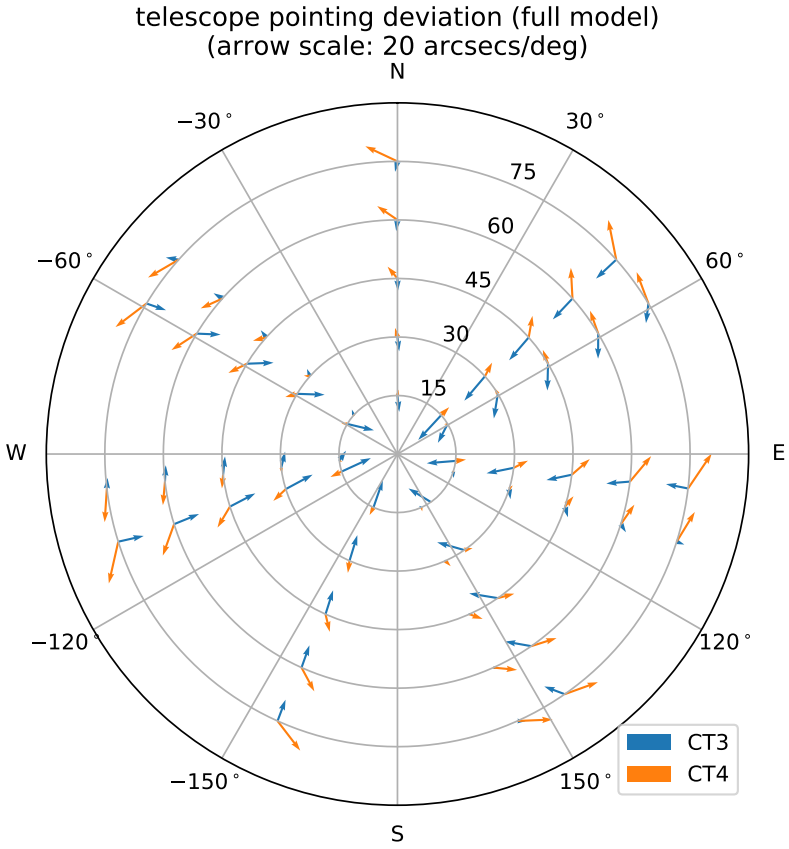

Figure 2.2: Example of a pointing model for CT3 and CT4, measured in 2020. The plot clearly shows that the pointing error varies widely for different values of altitude and azimuth and is unique for each telescope. This figure was created by the author, using software from the H.E.S.S. collaboration.

lid. Even thought the mirror's dimensions might seem arbitrary, we will later see why they are necessary. The mirror provides the space to achieve appropriate path lengths for the optical setup without having to go 'underneath' the lid. After passing the mirror, the light takes its way through a $2\,\mathrm{inch}$ optical system, which will be designated as 'the camera' in this work. Here it is first parallelized using a $-7.5\,\mathrm{cm}$ diverging lens (Thorlabs LC1315-A). The parallel light then passes an interference filter (Alluxa LC-HBP465/2-50) of $465\,\mathrm{nm}$ with an optical width of $2\,\mathrm{nm}$ FWHM to ensure that the light is almost monochromatic[1]. It is of important to notice that the light needs to be parallel at the interference filter, as it only filters the right range if hit perpendicular to its plane. The filtered light is then focused using a $f = 10\,\mathrm{cm}$ converging lens (Thorlabs LB1630-A) and fed into a non-polarizing beamsplitter (Thorlabs BS031), which equally divides the stream of photons onto two PMTs (modified version of Hamamatsu R11265U-300) with an sensitive area of $23\,\mathrm{mm}$ x $23\,\mathrm{mm}$ (compare fig. 2.3). Even though an intensity interferometry setup only requires a single PMT per telescope, the second PMT is included to provide a constant measurement of $g^{(2)}$ for the $b = 0\,\mathrm{m}$ baseline. These measurements can be used for testing and calibration. The beamsplitter can also be illuminated by a halogen lamp, which is fitted to the side of the beamsplitter housing. The halogen lamp can be used for reference measurements but is of no further importance for this work.

Even though this optical setup is quite efficient at getting an incoming perfect light cone filtered and measured, its performance sinks drastically if the light hits the first lens at an angle or if the central ray of the cone is not aligned with the axis of the optical system. Additionally, it is crucial that the path length is adjusted correctly so that the lens sits at the correct 'depth' within the cone. As the focal point of the cone should be the same as the one of the converging lens, one can easily understand, that the lens should be $7.5\,\mathrm{cm}$ in front of the telescope's focal plane. The impact of a misplacement of the lens respectively non-optimal entry conditions of the light into the optical system has been investigated by Sebastian Konrad in his Master thesis [15]. Through extensive simulations, he was able to show that whilst the light path and especially the behavior of the interference filter are of quite complicated nature, the resulting rate as measured by the PMTs is not only a good measure for the transmission of the system but also indicates whether the light was filtered sufficiently well by the interference filter. When trying to optimize the overall performance of the system, it is therefore reasonable to only optimize for a high rate. To ensure a good performance of the optical system, it is supplemented by a mechanical system that can be used to alter the light path in different ways.

[1] Deciding on the width of the filter is a compromise between photon statistics and the signal size. While a wider filter allows more photons to pass, which leads to better statistics, the increasing width of the filter also results in a smaller correlation signal. In the used setup the optical width of the filter is comparatively small but in the lab proved to be well working in this application.

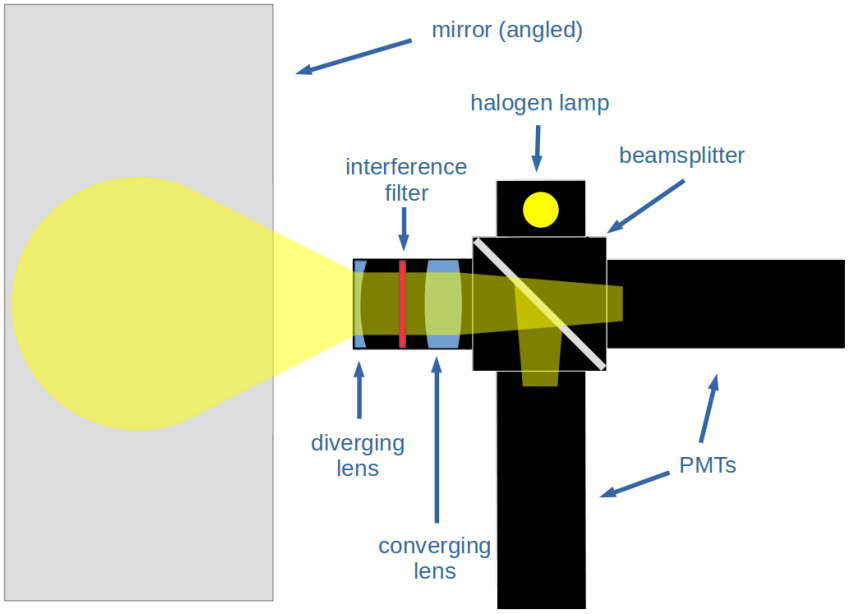

Figure 2.3: Schematic drawing of the optical setup.

2.2.2 Optimization of the Light Path

Before going into the details of the mechanical setup, we first need to establish which challenges, posed by the telescope and the optical setup, it needs to correct for. As there is no possibility to change the point-spread function (PSF) of the telescope, we will primarily describe the incoming light beam with respect to its central ray.

- **position of the focal plane / path length (1 degrees of freedom (DoF)):** The point where all the rays from the light beam converge into one point is the focal point, which - with considerations of the optical system - should be placed in the ideal spot. While theoretically this spot is easy to calculate and constant over time, the focal length of the telescope might change, for example because of the misalignment of the facets due to gravitation.

- **x- and z-position in the focal plane (2 DoF):** To understand the nomenclature, it is helpful to imagine sitting in the center of the dish and looking onto the camera respectively the lid (compare fig. 2.4). The z-dimension is a horizontal axis with the positive direction to the left and the x-direction is the vertical axis with its positive direction upwards. These two DoFs correspond directly to the miss pointing of the telescope in azimuth (z-direction) and altitude (x-direction). Therefore, one can be sure to find substantial need for adjustment in these two dimensions (compare fig. 2.2).

- **angle of the incoming light relative to in the focal plane, α and β (2 DoF):** As the central ray is supposed to hit the optical system perpendicular to the first lens, we have to consider the angle of the incoming light and correct for it. We therefore define the angle α as the deviation of the angle between x-axis and the central ray from $90°$ and β as the deviation of the angle between z-axis and the central ray from $90°$. While a need to correct in these two dimensions might seem unlikely, it would still be possible that corrections are needed: Due to the weight of the camera ($\approx 900\,\mathrm{kg}$) and its holding arm, the upper side of the arm might be stretched and the lower side compressed for pointing positions close to the horizon, leading to a tilting of the camera's lid relative to the dish.

From this we can conclude that one has to consider up to five independent degrees of freedom (DoF) that need to be controlled by the mechanical setup.

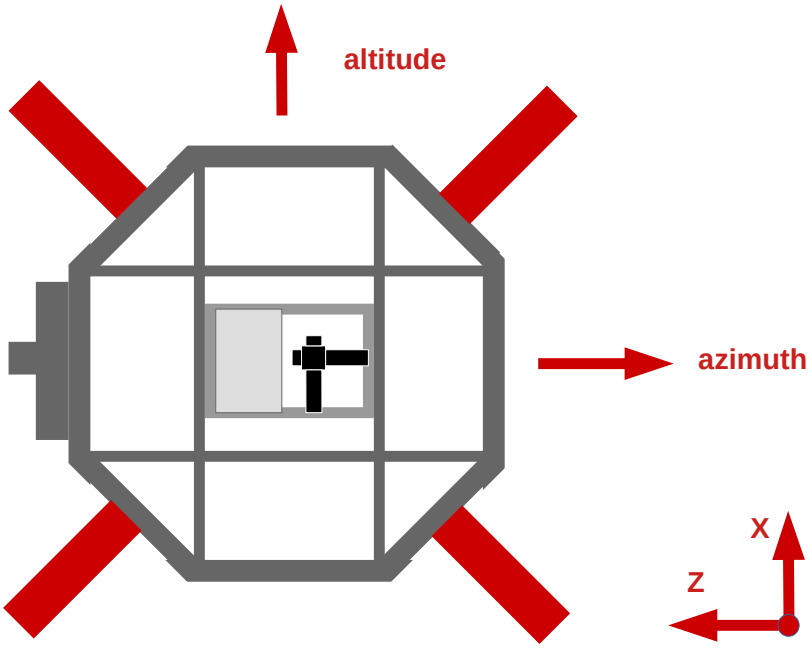

Figure 2.4: View onto the lid as seen from the center of the dish. The central hexagon is the lid, with the optical setup in its center. The red steel rods in the corners are part of the arm that holds the camera in place.

2.2.3 Mechanical Setup

As mentioned before, the optical system needs to be adjusted to deliver the desired performance. As the misspointing of the telescope changes over the time of the measurement (as the position changes), it needs to be able to adjust on the fly during the measurements. It therefore consists of six servo motors that allow the optical setup, especially the mirror, to be moved to different positions within seconds.
The coordinate system for these adjustments, as well as an overview of the setup itself, can be found in fig. 2.5.

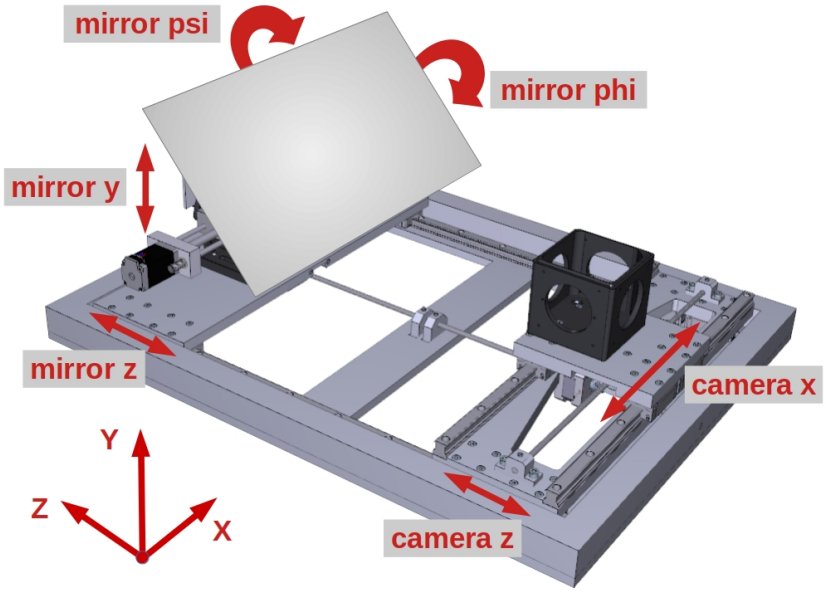

Figure 2.5: Schematic drawing of the mechanical setup. Note that parts of the optics are not shown in this sketch for clarity.

The **mirror** can be moved in four degrees of freedom:

- z**-direction:** The movement in the z-direction is achieved by a servo motor (Nanotec SC2818L1504-B) which is mounted on a spindle. As the whole mirror-part of the setup is placed on a sled with rails in the z-direction, it can freely move in a range of about $130\,\mathrm{mm}$, allowing for good adjustments in the z-direction. Note that a change of the mirrors z-position does not only allow to correct for the z-dimension of the central ray, but also has an impact on the path length of the light before being fed into the camera.

- **y-direction:** The movement in the y-direction (perpendicular to the lid plane) is achieved by a labjack (Thorlabs L490) fitted with a servo motor (Nanotec SC2818L1504-B) and an additional gear (Nanotec GPLL22-5) for extra strength, which allows the distance between the mirror and the lid to be changed from the theoretically best position by $-15\,\mathrm{mm}$ to $10\,\mathrm{mm}$. Even though driving speed is the slowest of all dimensions in terms of $\frac{\mathrm{mm}}{\mathrm{s}}$, it is still sufficient as we will see later on. Note that this DoF of the mechanical setup is not strictly tied to any of the parameters of the light beam that were described in section 2.2.2.

- **Φ-direction:** The mirror is held by an optical mount (standa 8MUP21-2), which allows for a tilting of the mirror from $-4.5°$ to $4.5°$ from the axis with a resolution of $<1\,\mathrm{as}$ using a stepper motor. A correction of this parameter (away from the zero position) allows to correct for slanting light, or to be precise, for an α of the incoming central ray. The Φ-direction is therefore defined by its rotation around the y-axis of the setup.

- **Ψ-direction:** The tilt in the Ψ-direction is achieved similarly to the one in the Φ-direction and serves the same purpose, only that now we correct for the slanting angle β. Therefore the Ψ-direction is defined as the rotation around the x-axis of the setup

To fully understand the range in which Camera Z and Mirror Z can operate, one needs to know that a minimum distance between them cannot be underrun. This is ensured by an electrical switch button, which is pressed as the two wagons approach each other.
Additionally the **camera** can be moved in two degrees of freedom:

- **z-direction:** The movement in the z-direction is achieved by a servo motor (Nanotec SC2818L1504-B) which is mounted on a spindle. It can move in a range of about $130\,\mathrm{mm}$, allowing for sufficient adjustments in the z-direction. This dimension is therefore the primary one when it comes to correcting the path length of the light.

- **x-direction:** The movement in the x-direction is achieved by a servo motor (Nanotec SC2818L1504-B) which is mounted on a spindle. It can move in a range from about $-120\,\mathrm{mm}$ to $120\,\mathrm{mm}$ from the assumed zero point, allowing for good adjustments in the y-direction. As the mirror cannot be moved in the x-direction, this is the only way to adjust for any misspointing in the x-direction. The fact that the mirror cannot be moved in the x-direction is also the reason for its large width in the x-dimension, as it needs to be able to cover the whole x-range without being moved.

To allow for reference measurements without light and protect the optical system during daytime, there is a movable shutter fitted to the entry of the optical system. It can gradually be opened and closed using a $180°$-servo motor.

2.3 Electronics and Computing

The electronics involved in this experiment can be separated into two parts: measurement and control electronics.

2.3.1 Measurement Electronics

These electronics are used to measure the incoming photons. They consist of a so called 'camera unit' which is placed at the camera of each telescope and the central workstation that is connected to the camera units via fibers. Let us start with explaining the electrical setup at the camera unit.
The camera unit consists of three main parts

- **Amplifiers and cables** The amplifiers sit close to the PMTs and are not placed inside the housing of the camera. They have their own powersupply attached to them and preamplify the signal from the PMTs by a factor of 10. After being amplified, the signal from one of the PMTs is fed through a $10\,\mathrm{m}$ coax cable, the other one through a $40\,\mathrm{m}$ coax cable. This different length of the cables is chosen to shift the bunching peak in the temporal $g^{(2)}$ function out of the $\tau = 0$ region, where card-crosstalk disturbs the measurement.

- **Sampling Card** The sampling card (Spectrum Instrumentation M4i.2211-x8) samples the signals from the PMTs. Each camera unit has one such card installed. It allows for $8\,\mathrm{bit}$ sampling with up to $0.8\,\mathrm{ns}$ time resolution on two channels. For this experiment a time resolution of $1.6\,\mathrm{ns}$ is sufficient and therefore used, as it saves valuable disc space. Furthermore, the sampling card is connected to the white rabbit system of the telescope, which offers a $10\,\mathrm{MHz}$ clock and a $1\ \frac{\mathrm{pulse}}{\mathrm{second}}$ trigger, used for time synchronization.

- **PCI express** [2] **expander** A PCIe expander (adnacom S31) is used to forward the signal from the sampling card to the workstation. It is connected to the workstation by two single mode fibers.

At the **workstation**, the signals from both camera units are received and processed. It is therefore placed in the server room of the H.E.S.S. control building, where all the fibers from the telescopes terminate. During measurement this workstation records the signals from both sampling cards onto large RAIDs [3]. As each telescope produces $1.25\ \frac{\mathrm{GB}}{\mathrm{s}}$, a RAID 0 configuration is used to achieve sufficient writing speeds. In addition to writing the incoming signals to disk, the

[2] PCI express (or PCIe) is an abreviation of 'Peripheral Component Interconnect Express'. It is a standard to connect peripherals to the main chipset of a computer and is widely used in modern computers.

[3] RAID is the abreviation for 'Redundant Array of Independent Disks'. A RAID therefore consists of individual disks which are accessed through a RAID controller. In the used configuration (RAID 0) the RAID controller 'strips' the incoming data and writes the resulting chunks on different disks simultaneously. This results in a writing/reading speed that is the sum of the writing/reading speeds of each drive .

workstation also calculates the current rate as measured by each PMT. This rate is then passed on via Ethernet to the control boxes which require this information for rate optimizations.

2.3.2 Control Electronics

As the name suggests, these electronics are used to control the setup and make modifications to its state during the measurements. All of them are mounted on the lid next to the setup. The main unit is called 'camera box'. It consists of a Raspberry Pi 4 micro-computer which controls a 6-channel motor board (Trinamic TMCM-6214) to drive all the servos described in section 2.2.3. Additionally the Raspberry Pi controls the shutter through its GPIO[4] pins and is connected via USB to the so called 'halogen box' which turns the halogen lamp on and off and adjusts its brightness. The whole camera box and its peripherals can be managed from afar, as the Raspberry Pi has an Ethernet connection to the camera-network. This is usually done via VNC [5] from another machine in the camera-network. Also note that the motor box receives the current rate for each PMT from the workstation.
Furthermore, there is a high voltage power supply (CAEN 5533EN) installed in each camera, which supplies the PMTs with sufficient voltages. It is connected to the Ethernet as well and accessible over telnet.

[4] GPIO is an abbreviation for 'General Purpose Input Output'.

[5] Virtual Network Computing (VNC) is a software to visually control a remote computer. It forwards the content of the screen and allows for remote usage of mouse and keyboard of the accessed machine.

Chapter III

Algorithms and Implementation

3.1 AQO Motor Control Software

In order to control the motors of the mechanical setup, a software (referred to as 'motor control' in this work) was developed by the AQO group using *python* and the *pyTMCL* library [16]. It allows for manual control of each motor (compare section 2.2.3). Additionally, it provides the user with extra functionality, like opening and closing the shutter, saving motor positions and going back to them as well as some features for optimizations, which will be explained in the upcoming sections. One more core feature of the motor control is to connect to the workstation and get live rate counts from there via TCP/IP. A screenshot of the motor control's user interface is shown in fig. 3.1.

Figure 3.1: User interface of the motor control.

3.2 Modes of Measurement

It was established in section 2.2.3 that even though there are only 5 DoFs in the optical setup, there are 6 DoFs in the mechanical system. Additionally, there is the rate parameter which one wants to optimize. To get an intuition for different parameters, their behavior and correlations, it is oftentimes helpful to find a visible representation of the measured data. Hence, the author decided to develop measuring modes which each vary two DoFs, and plot the rate over the resulting two-dimensional grid, using heat-maps. The choice of combinations of these parameters was taken with some physical considerations, which will be explained in the following.

3.2.1 Z-X Mode

As established before, misspointing in both altitude and azimuth of the telescope is expected (see section 2.1.1, section 2.2.3). This corresponds to the x and z dimensions in the coordinate system of the setup. Due to the misspointing shown in fig. 2.2, one expects the need for extensive optimizations to direct as much light as possible into the optics. Hence, a measurement mode was developed that allows for a measurement and plotting of the rate while both X and Z

dimension are varied (compare fig. 3.3).
One can see, that the construction of the mechanical setup (compare fig. 2.5) does not allow for a change of the mirror's X position. Instead Camera X is used to scan through the range of possible X positions. The width of the mirror $400\,\mathrm{mm}$ was chosen such that it can cover all possible x positions of the spot without being moved

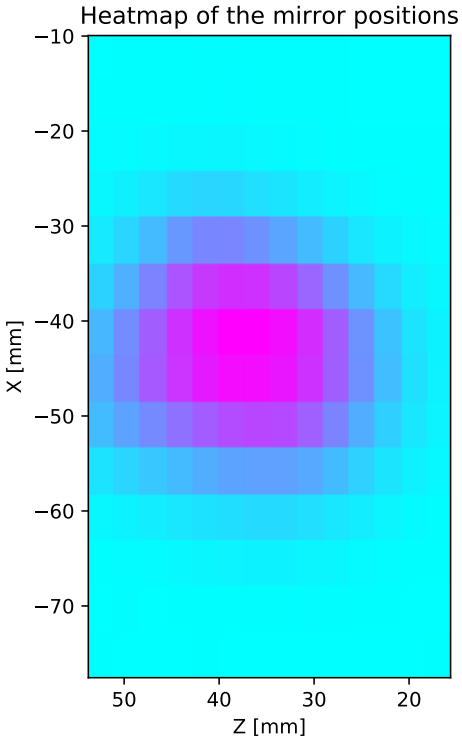

Figure 3.2: Heatmap, created by a Z-X scan. The zero point of each axis is defined just before the scan. This allows the user to see how far away from their initial guess the maximum lies, without having to worry about the absolute positions.

The variation of the Z position is achieved by moving Camera Z and Mirror Z simultaneously. This is necessary to prevent a variation in the light's path length.
The range of an Z-X scan is limited by the range the motors can move. For the X dimension the range of motion is $\approx 240\,\mathrm{mm}$, for the Z dimension $\approx 130\,\mathrm{mm}$.
For each measurement one needs to input the following values:

- **X center:** This is the zero point of the X-scale used for the scan. It is given in absolute values of camera X.
- **X min:** Lower limit of the X-scale to be reached during the scan.
- **X max:** Upper limit of the X-scale to be reached during the scan.
- **X spacing:** The spacing parameter defines how many measurements points are taken in each 'line' of X movement. It therefore (together with Z spacing) defines the 'resolution' of the heatmap.
- **Z center:** This is the zero point of the Z-scale used for the scan. It is given in absolute values of mirror Z.
- **Z min:** Lower limit of the Z-scale to be reached during the scan.
- **Z max:** Upper limit of the Z-scale to be reached during the scan.
- **Z spacing:** The spacing parameter defines how many lines of . It therefore (together with X spacing) defines the 'resolution' of the heatmap.

As one only wants to vary X and Z in this scan mode, all other parameters (Mirror Phi, Mirror Psi, Mirror Y, distance between Mirror Z and Camera Z) are set to a constant value before starting the scan. These preset parameters are determined experimentally in such a way as to allow light to reach the lens.
The procedure for the measurement is as follows:

- The software walks through the parameter-space line by line in the X dimension by varying Camera X.
- After each line, Camera Z and Mirror Z are moved and a new line is recorded. To save time, the variations of Camera X are running from negative to positive on even lines and from positive to negative on odd lines.
- For each combination of X and Z the rate, as transmitted by the workstation, is recorded.
- The resulting (X, Z, rate) triplet is then saved and used to create a heatmap (compare fig. 3.3).

During the measurement the heatmap is constantly updated, so that the user can see the progress of the measurement in real time.

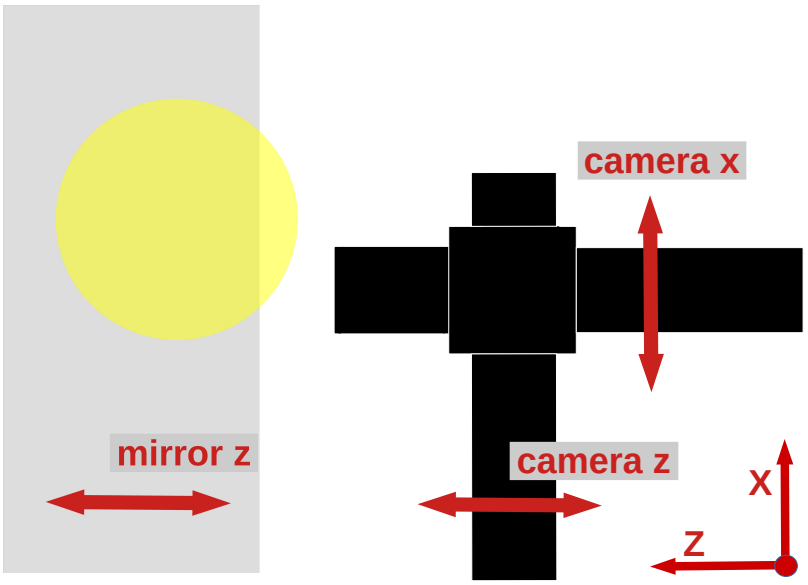

Figure 3.3: Schematic visualization of the Z-X mode.

3.2.2 X-Y Mode

The X-Y mode was implemented to optimize the Mirror Y parameter.As the name suggests, this mode of measurement varies the Camera X and the Mirror Y parameter. Similarly to the previous mode, **X center, X min, X max, X spacing, Y center, X min, X max** and **Y spacing** are set together with parameters which remain constant (Mirror Z, Mirror Psi, Mirror Phi, pathlength). As before, one wants to keep the pathlength of the light constant. However, every time the Y dimension is changed, this varies the distance between the dish and the setup's mirror. This change in pathlength is accounted for by varying the distance between camera and mirror, using the Camera Z motor, resulting a in constant pathlenght even though Mirror Y is changed. A measurement in X-Y therefore mode works as follows:

- The software walks through the parameter-space line by line in the X dimension by varying Camera X.
- After each line Mirror Y is varied according to range and spacing. Additionally, Camera Z is moved by the same distance as Mirror Y to correct the pathlength. To save time, the variations of Camera X are running from negative to positive on even lines and from positive to negative on odd lines.
- For each combination of X and Y the rate, as transmitted by the workstation, is recorded.

- The resulting (X, Y, rate) triplet is then saved and used to create a heatmap (compare fig. 3.4).

During the measurement the heatmap is constantly updated, so that the user can see the progress of the measurement in real time.

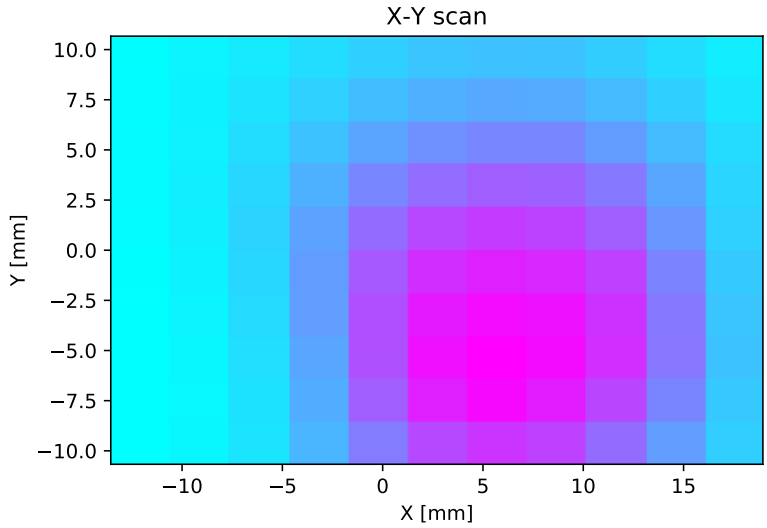

Figure 3.4: Heatmap, created by a X-Y scan. The scale of the axes is in mm, the zero point of each axes is defined just before the scan. This allows the user to see how far away from their initial guess the maximum lies, without having to worry about the absolute positions.

3.2.3 Phi-Psi Mode

The Phi-Psi mode is used to investigate how a tilting of the mirror effects the rate. As mentioned in section 2.2.2, it is crucial that the central ray hits the first lens of the optical setup perpendicular to its plane. To ensure this, it is helpful to measure the rate in dependence of Mirror Psi and Mirror Phi. Like in the other modes, **Psi center, Psi min, Psi max, Psi spacing, Phi center, Phi min, Phi max** and **Phi spacing** are set and the constant parameters (Mirror Z, Mirror Y, Camera Z, Camera X) are set before the measurement starts. The measurement is straight forward:

- The Psi dimension is varied according to Psi center, Psi min, Psi max and Psi spacing.
- After each line (movement of the mirror in Psi direction), Mirror Phi is moved by one step (according to Phi center, Phi min, Phi max and Phi spacing). To save time, the variations

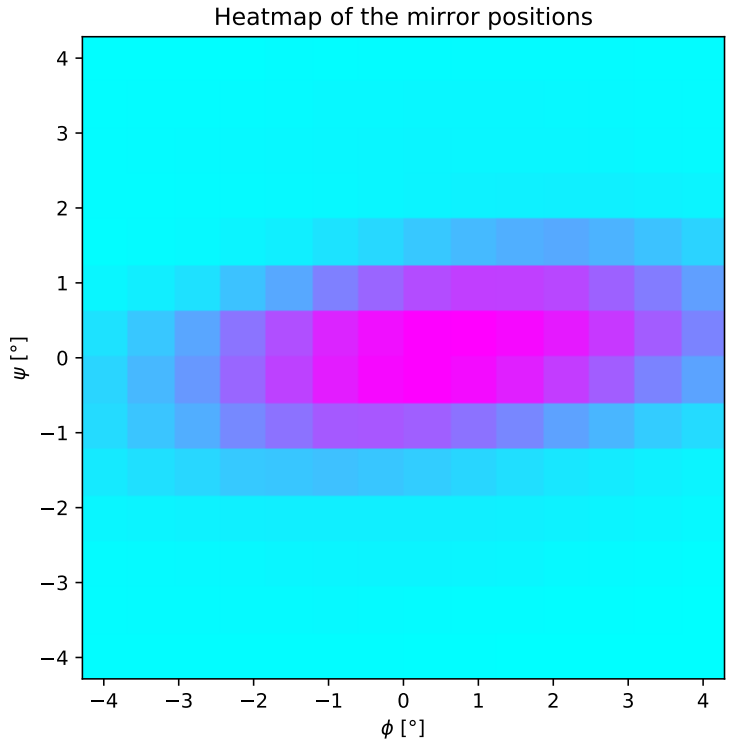

Figure 3.5: Heatmap, created by a Phi-Psi scan. The scale of the axes is in °. The zero point of each axis is defined by the geometry of the setup. Phi is equal to 0 when the edge of the mirror is parallel to the first lens, Psi is 0 when the angle between lid and the mirror plane is 45 °.

of Mirror Psi are running from negative to positive on even lines and from positive to negative on odd lines.

- For each combination of Mirror Psi and Mirror Phi the rate, as transmitted by the workstation, is recorded.
- The resulting (Phi, Psi, rate) triplet is then saved and used to create a heatmap (compare fig. 3.5).

During the measurement the heatmap is constantly updated, so that the user can see the progress of the measurement in real time.

Chapter IV

Evaluation of and Adjustments to the Software Performance

The measurements as taken in the different modes (X-Y, Z-X and Phi-Psi) each contain different information about the light path and possible corrections. But only extensive testing in the lab and on the telescope can lead to a stable routine, that automatically optimizes the parameters. Therefore, different lab measurements were conducted before creating an optimization routine for productive work in the telescope.

4.1 In the Lab

4.1.1 Lab Setup

The aim of the lab measurements was to create a test environment close to the later measurments on the telescope . Hence, a lab setup was built that provided the following conditions:

- A lightcone that matches the one of the telescope in geometry and intensity.
- A mount for the intensity interferometry setup, that allows for changes in all of the DoFs described in section 2.2.2.
- Enough stability (over time) that it is possible to reproduce measurements.

A schematic of the lab setup can be seen in fig. 4.1 below. It consists of a blue Light Emitting Diode (LED) with a variable power supply to adjust the brightness, placed at a distance of $2409\,\mathrm{mm}$ from an a fresnel lens (ORAFOL SC943, $f = 502.1\,\mathrm{mm}$). This lens might be known to the reader as an 'IceACT lens', as these lenses are used in the IceACT telescopes as well. The LED together with the lens create a light cone of similar geometry to the one found in the HESS phase 1 telescopes and thus a similar Point Spread Function (PSF). The focal point of

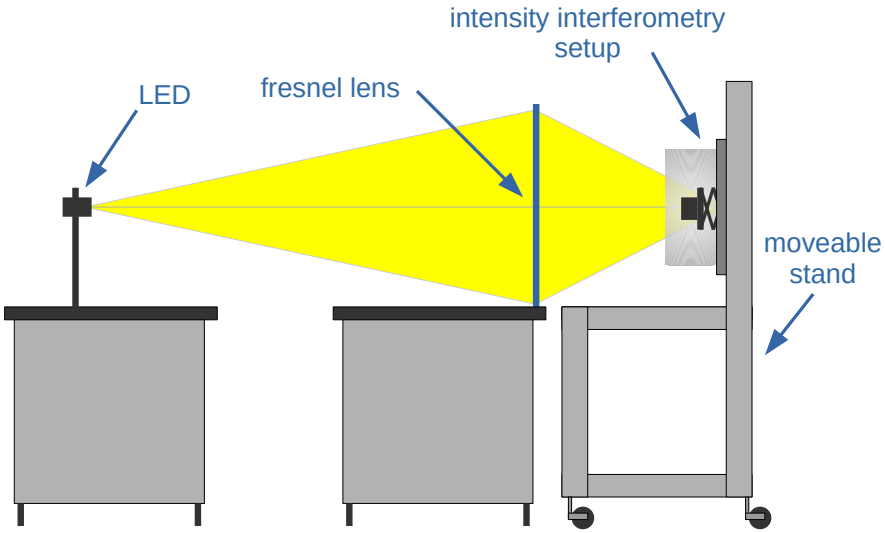

Figure 4.1: Lab setup as used for all lab measurements. The light originates in the LED on the left side. It is then focused by the fresnel lens and led onto the intensity interferometry setup. As the intensity interferometry setup is mounted on a movable stand, it can be rearranged in all different positions to simulate different conditions of the telescope.

the light cone is at $634\,\mathrm{mm}$ from the fresnel lens. Hence, the intensity interferometry setup was placed at that distance on a movable stand that allows for movement in all three translational dimensions, as well as two rotational dimensions.

4.1.2 Z-X Measurements and Their Interpretation

In the first step of lab measurements, the measurement modes (compare section 3.2) were all tested. Typical measurements as produced with each mode, can be found in fig. 3.3, fig. 3.4 and fig. 3.5.

The distribution (also refered to as 'spot') shown in each heatmap is identified to be elliptical in shape. It is also clear that the intensity is highest at the center of the ellipse and decreases as one moves outwards.

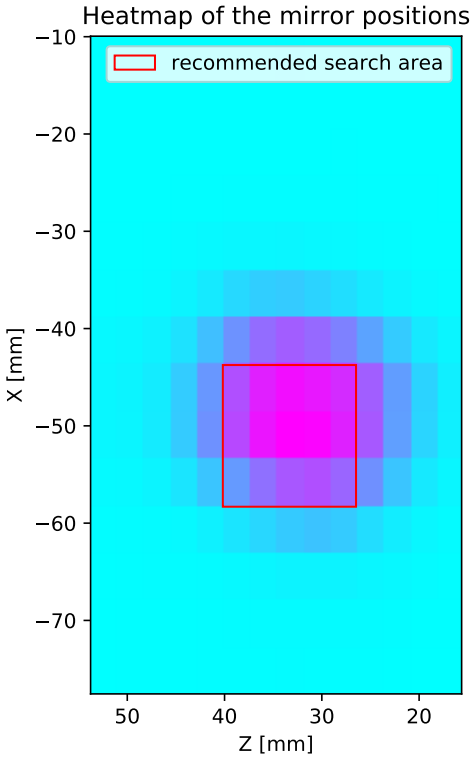

(a) In the first step of the analysis a rectangle is drawn around the brightest datapoints in the heatmap.

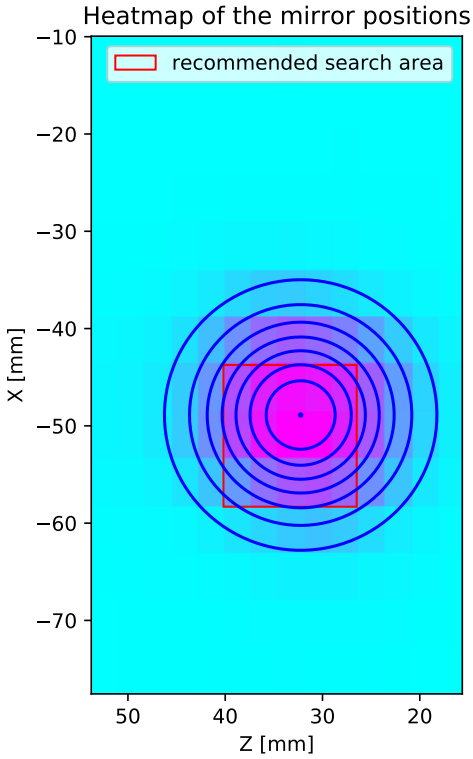

(b) In the second step of the analysis, a gaussian is fitted to the data. The starting parameter for the fit are determined from the first step (parameters of the rectangle).

Figure 4.2: Two step analysis of a heatmap.

Optimizing the rate means finding the value for each of the parameters, at which the highest rate is achieved. Hence, it would be beneficial to automatically find the highest intensity in each heatmap. Due to statistical fluctuations and the limited scan resolution it is not sufficient to select the parameter pair with the highest rate. To this end, a two step analysis was developed (compare fig. 4.2).
In the following, the algorithm is explained using the example of the Z-X measurement. Nevertheless, this algorithm can be applied to any heatmap. Depending on the scan to which this method is applied, one has to exchange these axes for the respective dimensions.

- **rectangular maximum finding:** The first step to finding the point of the maximum rate, is to select the area of the heatmap which shows the highest rate. To allow for some

flexibility this function gets an input parameter, called the 'contrast factor' (> 1) to adjust its sensitivity. The function then does the following:

- The highest rate present in the heatmap is determined.
- All pixels which display a higher rate than the threshold of $\frac{\text{maximum rate}}{\text{contrast factor}}$ are selected.
- A rectangle is drawn that includes all of the selected pixels. As the mask of the selected pixels commonly is not rectangular, this rectangle also includes pixels that are below the threshold.

This already limits the area which needs to be investigated closely.

- **2D Gaussian:** In this step, a two dimensional gaussian is fitted to the heatmap. The used function for the rate R is

$$R(x, y) = A \cdot \exp\left(-\frac{x - x_0}{2{\sigma_\text{x}}^2} - \frac{z - z_0}{2{\sigma_\text{y}}^2}\right) + B \tag{4.1}$$

The fit is done using a χ^2-fit, performed by the python function *curve fit* from the package *scipy.optimize*. A fit with this many free parameters will only converge if the optimization starts with reasonably guesses for each parameter. Therefore, the following starting parameters are used:

- x_0, z_0: The center of the rectangle from the previous step.
- σ_x, σ_z: half of the rectangle's width, respectively height.
- A: The maximum rate in the heatmap.
- B: set to 0.

These parameters have proven to usually lead to a converging fit. The resulting fit parameters now offer some interesting information:

- x_0, z_0: These values can now be considered the optimal value in the x and z dimension.
- σ_x, σ_z: The width/height of the gaussian is a good indicator of how focused the light beam is at the measured position. While small values of σ_x, σ_z imply that the lens is quite close to the optimal focus, large values imply that the distance between lens and mirror still needs some optimization.
- $\frac{A}{B}$: This value is a rough indicator for the $\frac{\text{signal}}{\text{background}}$-ratio.

The process of determining the optimal values of x_0 and z_0 using the above algorithm is surely more complex than just taking the x and z value of the pixel with the highest rate. However, it is

more precise, as it includes the information from all the pixels around the brightest spot. Additionally, it is also more robust to fluctuations in the rate and offers some additional information, as we have just seen.
Using the above algorithm on Z-X scans proved to allow for good positioning of Camera X and Mirror Z.
Depending on the exact parameters (range and especially spacing of X and Z), this measurement typically takes about $1 - 5$ minutes.

4.1.3 X-Y Measurements with Variable Camera Z

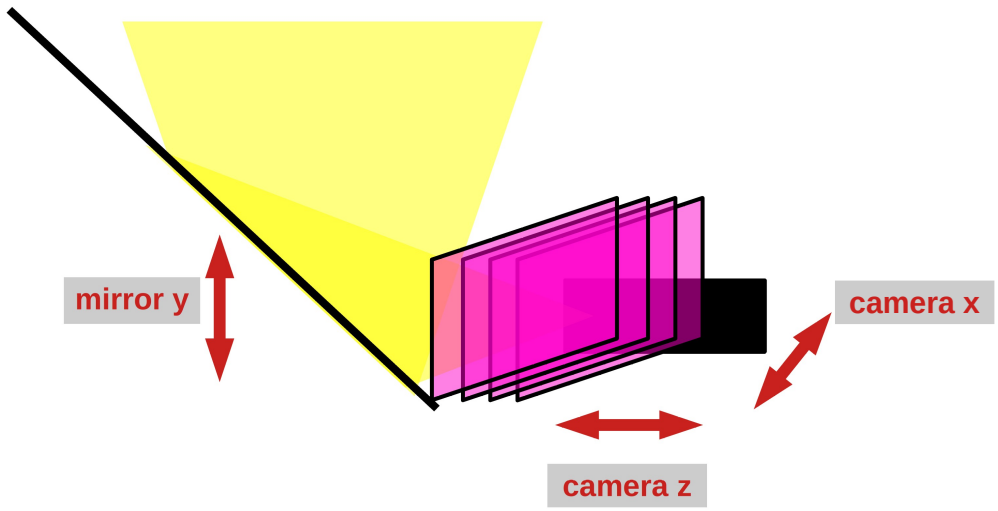

Figure 4.3: Visual representation of X-Y measurements with variable Camera Z. Multiple X-Y scans are recorded at different distances of the camera from the mirror. The results of these measurements can be used to gain a better understanding of the light beam's geometry.

As good values for Camera X and Mirror Z were determined in the previous section, one now wants to find good values for Camera Z, Mirror Phi and Mirror Psi. To fulfill that task, a series of scans is performed to closely investigate the geometry of the light beam. This can be achieved by doing multiple X-Y scans, while moving the camera closer and further from the mirror, using Camera Z (compare fig. 4.3).

The measurements are conducted using the following parameters:

- **Mirror Psi and Mirror Phi** are set to 0.
- **Spacing X and Spacing Y** are set to 24 to ensure a good resolution of each individual X-Y scan.
- **Range X** are set to $\pm 20\,\mathrm{mm}$, as previous experience shows that this range is sufficient
- **Range Y** are set to $\pm 10\,\mathrm{mm}$, because even though a larger range would be nicer for the measurement, the range is limited to about $\pm 10\,\mathrm{mm}$ by the movability of the labjack.
- **Camera Z** was adjusted in steps of $5\,\mathrm{mm}$ from $15.5\,\mathrm{mm}$ to $70.5\,\mathrm{mm}$, which is the whole range that was possible given the movablity of Camera Z.

Fig. 4.4 and fig. 4.5 show the X-Y scans at the outermost points of the Camera Z range. One can clearly see, that the center of the spot moves upwards as the camera moves away from the mirror (smaller Camera Z). It is also apparent, that the spot seems to 'wash out'. To better quantify that 'movement' and 'change in shape', a gaussian was fitted to each X-Y scan. The resulting values for the center of the spot (x_0, y_0) and the width/height of the spot (σ_x, σ_y) as well as the maximum intensity (given by the A parameter of the fit) were plotted against the Camera Z value of each scan (for a detailed explanation of the parameters see eq. (4.1)).

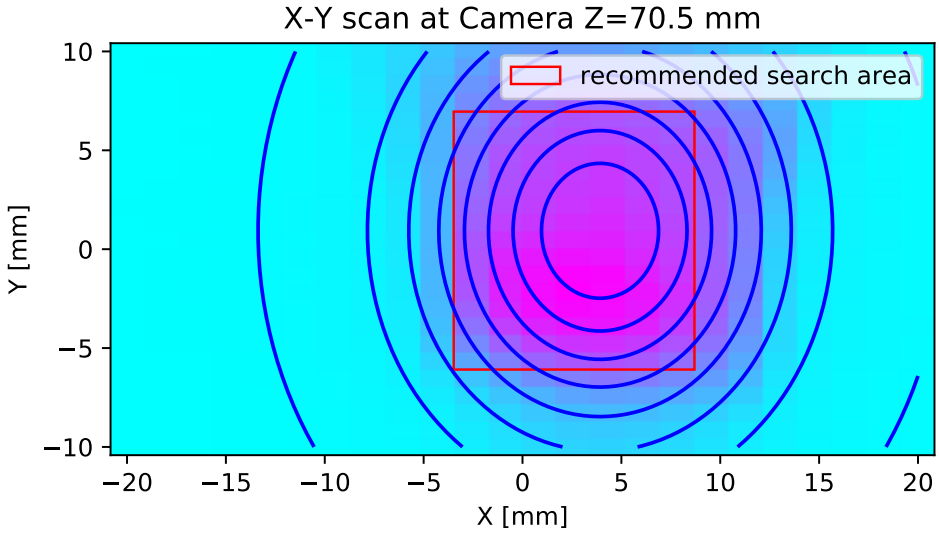

Figure 4.4: Heatmap, created by a X-Y scan at Camera X =70.5 mm.

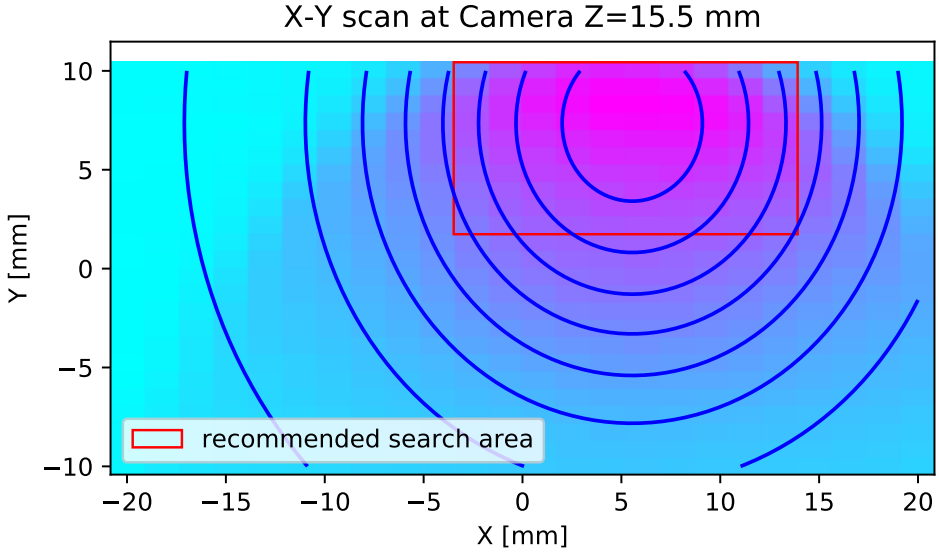

Figure 4.5: Heatmap, created by a X-Y scan at Camera X =15.5 mm.

Combining the Camera Z value from each one of the X-Y scans and the parameters of their gaussian fits, allows for some interesting observations. Looking at fig. 4.6 and fig. 4.7, one can clearly see, that both x_0 and y_0 seem to decrease linearly as the camera is moved closer to the mirror. It is therefore reasonable to assume, that the light beam does not hit the plane of the lid perfectly perpendicularly but at an angle.
Using the slope c of the fitted linear functions ($x_0 = c \cdot Z + t$), one can use simple trigonometry to calculate the angle of incidence $\gamma_\mathrm{n} = \arctan(|c|)$.
The slopes c as well as the calculated angles of incidence γ can be found in table 4.1.

dataset	c	γ [°]
x_0	$(-31.3 \pm 1.5) \cdot 10^{-3}$	1.79 ± 0.09
y_0	$(-111 \pm 13) \cdot 10^{-3}$	6.33 ± 0.68

Table 4.1: Slopes of the linear fit to the data shown in fig. 4.6 and fig. 4.7 and their respective angles of incidence γ.

The calculated angles γ_x and γ_y correspond to $\alpha = \gamma_x$ and $\beta = \gamma_y$ as defined in section 2.2.2. Therefore, one can actually use this method to investigate these two parameters. The values of $\alpha = (1.79 \pm 0.09)°$ and $\beta = (6.33 \pm 0.68)°$ also seem reasonable, given the imprecision of the lab setup.

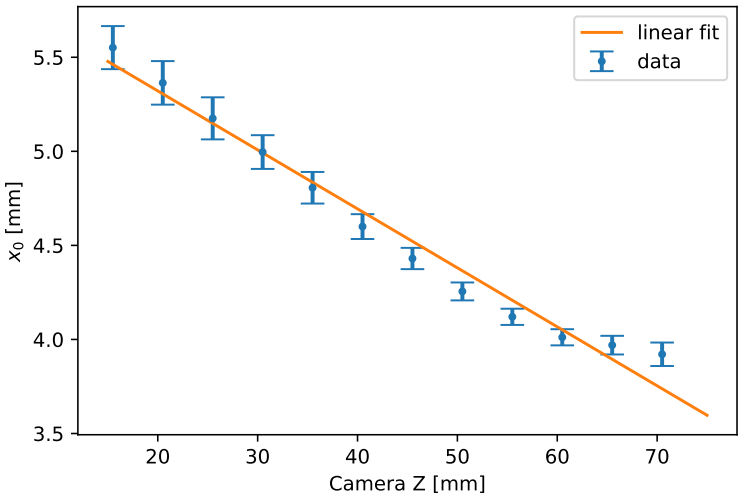

Figure 4.6: Plot of the fit parameter x_0 from different X-Y scans over Camera Z. One can easily see, that x_0 decreases as the camera moves closer to the mirror (increasing Camera Z). This slope of the linear fit is $c = (-31.3 \pm 1.5) \cdot 10^{-3}$.

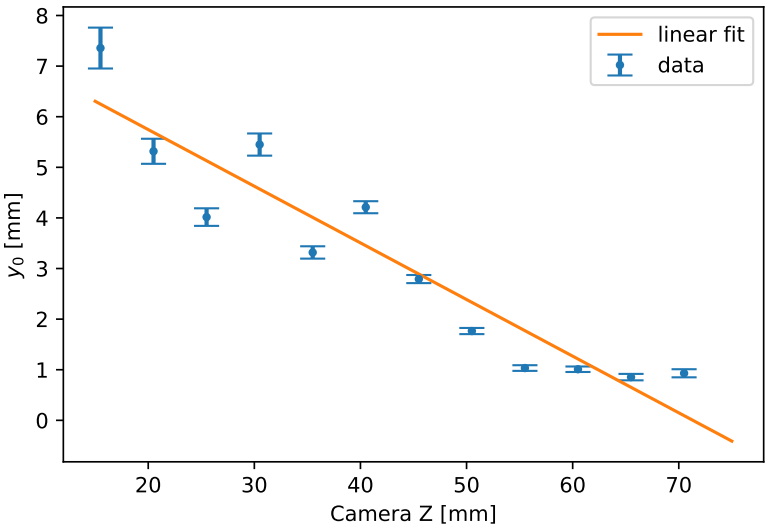

Figure 4.7: Plot of the fit parameter y_0 from different X-Y scans over Camera Z. One can easily see, that y_0 decreases as the camera moves closer to the mirror (increasing Camera Z). This slope of the linear fit is $c = (-111 \pm 13) \cdot 10^{-3}$. During the measurements, the calibration of the Mirror Y parameter had to be redone several times. This may lead to slight deviations of some data points from their actual position and can explain a too broad distribution of measurement parameters.

Plotting σ_x, σ_y over Camera Z (compare fig. 4.8, fig. 4.9), one can see how the shape of the spot changes. It is easy to see, that the smallest σ_x and σ_y are reached at a Camera Z of $\approx 60\,\mathrm{mm}$. Interestingly a plot of A over Camera X (compare fig. 4.10) shows that the maximal rate is also reached at $\approx 60\,\mathrm{mm}$. This makes sense as one expects the light beam to converge as it reaches its focal point.
Therefore, one can conclude that these parameters correlate with each other and optimizing one of these also leads to an optimization of the other two.

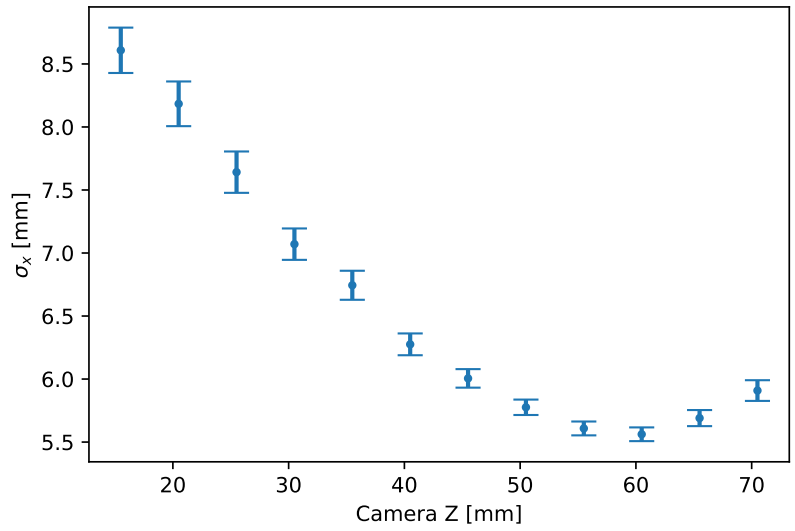

Figure 4.8: Plot of the fit parameter σ_x from different X-Y scans over Camera Z. One can clearly see, that the lowest value of σ_x is reached at $\approx 60\,\mathrm{mm}$.

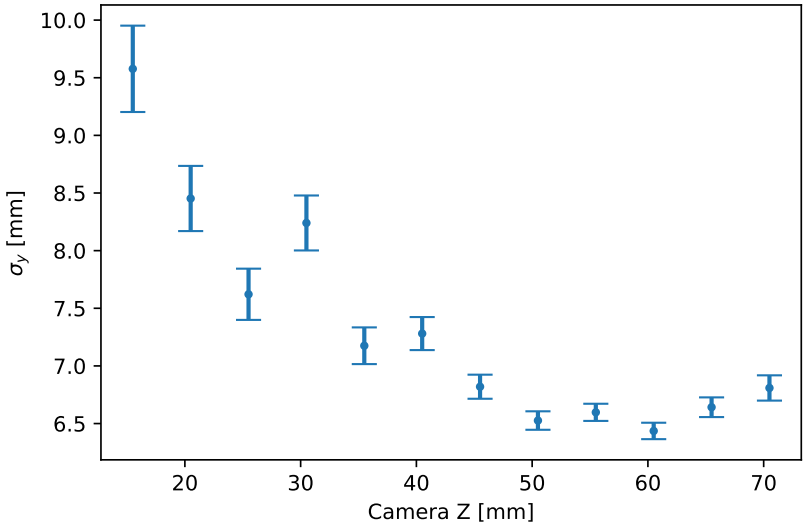

Figure 4.9: Plot of the fit parameter σ_y from different X-Y scans over Camera Z. One can clearly see, that the lowest value of σ_y is reached at $\approx 60\,\mathrm{mm}$.

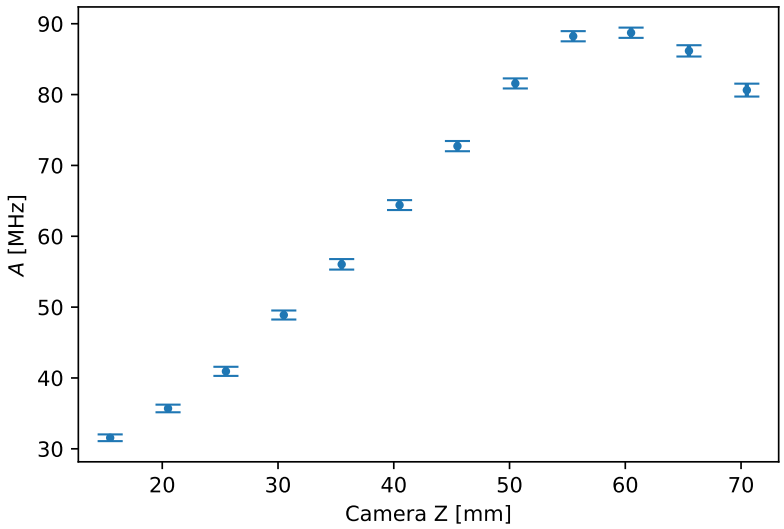

Figure 4.10: Plot of the fit parameter A, which corresponds to the maximal rate, from different X-Y scans over Camera Z. The maximal value of A is reached at $\approx 60\,\mathrm{mm}$.

To summarize these observations one can say the following for each parameter:

- x_0 and y_0: The slope of the linear dependency between x_0 and Camera Z or y_0 and Camera Z is an indicator for the angle at which the light hits the setup. One can therefore use this information to optimize Mirror Phi and Mirror Psi.

- σ_x, σ_y and A: Finding the minimum of σ_x, σ_y or maximum of A means finding the the maximal rate. Hence, this allows for an optimization of Camera Z.

The most valuable information gathered from this is the one about the angle at which the light beam hits the setup, as the information about the focus of the light beam can be obtained through another, less time intensive method (compare section 4.1.4).
Knowing the center of the gaussian (x_0, y_0) and its corresponding Camera Z value, it is easy to calculate the angle at which the setup is hit by the lightbeam (α and β, compare section 2.2.2). This angle can be corrected for by adjusting Camera Phi and Camera Psi, so that the lightbeam hits the first lens of the optical setup perpendicularly. The X-Y scans with variable Camera Z are therefore able to fully optimize Mirror Phi and Mirror Psi.
However, tilting the mirror in the Mirror Phi and/or Mirror Psi parameter also results in a change of distance, at which the central ray (respectively the light beam) travels parallel to the lid. Therefore, one has to finally adjust Mirror Y and Camera X by doing a single X-Y scan and

setting Mirror Y to the y_0 parameter of the fitted gaussian.

This procedure gives important insights into the geometry of the beam and helps to optimize many different parameters. However, it also also important to notice that it is quite time intensive, as each X-Y scan takes at least $5\,\mathrm{min}$ and that this time increases, if the resolution of the scan is increased.
The scan performed in this section took $\approx 15\,\mathrm{min}$ per X-Y scan, which multiplied with the number of 12 individual scans, leads to a measurement time of $\approx 3\,\mathrm{h}$. Therefore, this scan might be helpful to gain scientific understanding of the light beam but not for any optimization on the telescopes

4.1.4 Investigation of the Focal Point

In the case that all other parameters but Camera Z are already optimized, optimizing Camera Z becomes a one-dimensional optimization problem. Therefore, one can just walk through the range of feasible values for Camera Z and record the resulting rate. An example of this is shown in fig. 4.11.

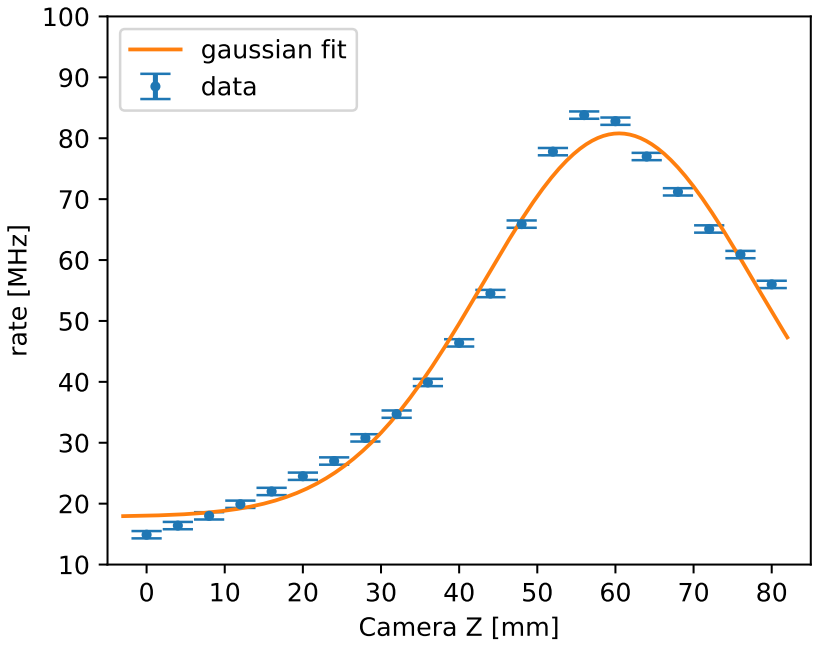

Figure 4.11: Plot of the measured rate over Camera Z. All other parameters are kept constant.

It is easy to see, that there is an optimal position for Camera Z. To find this optimal position a gaussian is fitted to the datapoints. Its fit parameters tell us, that the optimal rate is expected at Camera X ≈ 60 mm. However, as the gaussian is only an approximation and it is apparent that the datapoints don't resemble a gaussian very well, it seems reasonable, to do a high resolution scan around the maximum of the gaussian and take the Camera Z position, for which the highest rate was measured as the optimal position.

With respect to time efficiency this scan is quite favorable. It can be performed in less than $1\,\mathrm{min}$ and yields the same information about the Camera X parameter as the procedure shown in section 4.1.3. Even if further optimization close to position of the gaussian's peak is done, this measurement is still a lot faster than doing an X-Y measurement with variable Camera X.

4.1.5 Summary of the Results from the Different Measurements

In the previous subsections (section 4.1.2 to section 4.1.4), different strategies to optimize individual parameters were presented. A summary about the different parameters and the respective measurements to conduct to optimize them is given in table 4.2. It shows that it is possible to optimize all 6 parameters, using the given strategies. In the practical labwork, it has proven to be easiest if the optimization is performed in the following order:

1. **Z-X scan** (compare section 4.1.2): Set Mirror Z and use the found Camera X as an approximation for the following steps.
2. **X-Y scans with variable Camera Z** (compare section 4.1.3): Set Mirror Phi, Mirror Psi in the first step and then Mirror Y and Camera X (now final value for camera X)
3. **Focus investigation** (compare section 4.1.4): Set Camera Z.

Note that the Psi-Phi measuring mode (compare section 3.2.3) is not needed to optimize all 6 parameters.

Parameter	Z-X (section 4.1.2)	X-Y (section 4.1.3)	Focus Inv. (section 4.1.4)
Camera X	✓		
Camera Z		possible but not efficient	✓
Mirror Z	✓		
Mirror Y		✓	
Mirror Phi		✓	
Mirror Psi		✓	

Table 4.2: Overview of which Parameters can be constraint by which measuring mode.

4.2 Automation of the Optimization Routine

To save time and make the final measurements of the intensity as efficient as possible, an automatic optimization routine was developed. The declared goal was to keep the operator of the intensity interferometry setup as far from the process of optimization as possible, to ensure easier operability.
On the other hand, the measurement time on the telescope is rare and it needs to used for measurements, as much as possible. Hence, the optimization routine also needs to be time efficient. This led to the conclusion not to use any X-Y measurements with variable Camera Z, as the information gathered through these measurements was not deemed valuable enough with respect to the needed time.
The challenge of optimizing the light flux in the optical system can be divided into two different cases:

- **initial optimization:** The initial optimization needs to be performed every time the telescope pointing changes by a larger amount. This is typically the case, each time the pointing is changes to a new source (star).
- **continuous optimization:** As the telescope moves while tracking the source, the misspointing of the telescope changes over time. Therefore, corrections need to be made to the pointing.

It is easy to identify that the initial optimization is a larger challenge than the continuous optimization, as one has less information about the misspointing. Therefore, the focus in this work has been set to the initial optimization. Using the experience obtained during the lab measurements, the following strategy was used to optimize the rate:

- **Z-X large:** In the first step, a rough overview over the position of the spot in the X and Z dimension is achieved using a scan in Z-X mode. As mentioned before, the parameters for this scan need to be defined sufficiently, so that there is a high chance of actually getting a good rate. Hence, the following constant parameters were chosen:
  - Mirror Psi: $0°$. As the central ray is expected to hit the focal plane perpendicularly, this value is a good starting point
  - Mirror Phi: $0°$. As the central ray is expected to hit the focal plane perpendicularly, this value is a good starting point
  - Mirror Y: $133\,\mathrm{mm}$. This value is the position of the mirror, which (considering the geometry of the setup) makes sure that the whole crosssection of the light cone is covered by the mirror, in the case of optimal X and Z values. It has also proven work well during the lab measurements.

- Distance between Mirror Z and Camera Z coordinates: $329\,\mathrm{mm}$. This value was chosen to make sure that the range of movement of both Mirror Z and Camera Z are fully usable during the scan. As the distance between Mirror Z and Camera Z is kept constant during this measurement, the issue of being 'in focus' or 'out of focus' is the same for all measuring points. Therefore, this parameter can be optimized in a later step of the optimization routine.

Additionally, the range of the measurement in both X and Z direction needs to be set. Here the following settings have proven advantageous:

- Z dimension: As stated when explaining the Z-X mode (see section 3.2.1), Camera Z and Mirror Z are moved simultaneously during the measurement. The staring point is set at $51\,\mathrm{mm}$ for Camera Z, respectively $380\,\mathrm{mm}$ for Mirror Z. The range of the scan relative to the starting positions runs from $-50\,\mathrm{mm}$ to $50\,\mathrm{mm}$. As the scan is used to get a quick overview over a wide parameter-space in the Z dimension, the spacing is set to 7 to reduce the time needed for this scan.
- X dimension: In the X dimension Camera X is moved. The starting position is set at $0\,\mathrm{mm}$ and the range is set from $-70\,\mathrm{mm}$ to $70\,\mathrm{mm}$. This ensures that even if large misspointing in the altitude is present, the scan finds the spot. As for the Z dimension, the spacing is set to 7 to reduce the time for the scan.

After the scan, a rectangle is drawn around the brightest measurements of the heatmap as described in section 4.1.2. Its position and size are used to derive the parameters for the next step of the optimization routine.

- **Z-X small:** This next step is used to find the final X and Z positions for the mirror. It operates similarly to the Z-X large scan but focuses on the area identified by the previous scan. While the constant parameters are kept from the previous scan, the scan parameters are adjusted:
  - Z dimension: The new starting position in the Z dimension is set at the center of the rectangle, as determined by the Z-X large scan. The total range of the scan in this dimension is calculated using the size of the rectangle and multiplying it by 1.5. In case this would exceed the range of movability of either Mirror Z or Camera Z, the range is reduced to the maximum possible position of the respective motor. The spacing is again set to 7.
  - X dimension: Starting position, range and spacing in the X dimension are set in the same way as in the Z dimension.

The resulting heatmap is then fitted with a 2 dimensional gaussian (compare section 4.1.2). The center of the gaussian (x_0, z_0) is then used to find the ideal X and Z, which are used to finally determine Mirror Z and Camera X.

- **Camera Z:** The last parameter to optimize is the distance between the mirror and the camera. This is done by varying the distance between Camera Z and Mirror Z ($329\,\mathrm{mm}$) by $\pm 20\,\mathrm{mm}$ in 30 steps and measuring the rate for each. The final value of Camera Z is then determined by using the Camera Z position at which the highest rate was measured.

Even though a long term goal would be complete automation of the whole optimization process (and consequently also the continuous optimization), only the initial optimization was implemented before the campaign. This was due to time constraints and the fact that such an automated routine would not be necessary at this stage of the project, as multiple operators would be there at any time.

4.3 On the Telescopes

4.3.1 H.E.S.S. Campaign

After extensive testing of the setup in the lab, the AQO group at ECAP decided to go to the H.E.S.S. site in Namibia for a test of the developed system. The campaign was carried out by Andreas Zmija, Naomi Vogel and the author from April 5th to April 25th 2022, which included both setting up everything at the H.E.S.S. site and an active measuring period from the 15th to the 23rd. The aim of the campaign was to test the experimental setup which was developed in the years prior, as well as to measure at least one star as a proof of feasibility. The primary targets for observations in this campaign were Acrux, Mimosa, Shaula, Nunki and Regor. As all the intensity interferometry measurements needed correct pointing, this also proofed to be a good opportunity to test the developed optimization routines.

4.3.2 Productive Spot Finding and Performance

The nightly observations during the campaign put the developed mechanical, electrical and computational system to a test.

Initial Optimization

Every time the pointing of the telescope was changed to a different object (and consequently at the beginning of each night), the initial optimization routine, as described in section 4.2, was performed.
The first step of the optimization (Z-X large) routine was always able to find the area of interest which contains the highest rates. From there also the second step (Z-X small) always recorded a heatmap which allowed for the fitting of a gaussian. Therefore, both Camera X and Mirror Z were easy to set at the right values. The third step of optimizing the distance between the camera and the mirror failed to some errors in the implementation. It was therefore decided to do this one-dimensional optimization manually, as this was seen as an easy task by the operators.

An example of a typical run of the optimization routine can be found in fig. 4.12. As one can see, the two steps of the optimization both make sense, as the first one allows to narrow down the area of interest in the parameter space. The second step with its greater resolution then allows for a precise fitting of a gaussian, resulting in the optimal parameters (compare table 4.3). Consistently, the value of Camera X was set to $x_0 = -9.74$ and Mirror Z to $z_0 = -2.47$. Afterwards, the optimal value for Camera Z was determined manually.

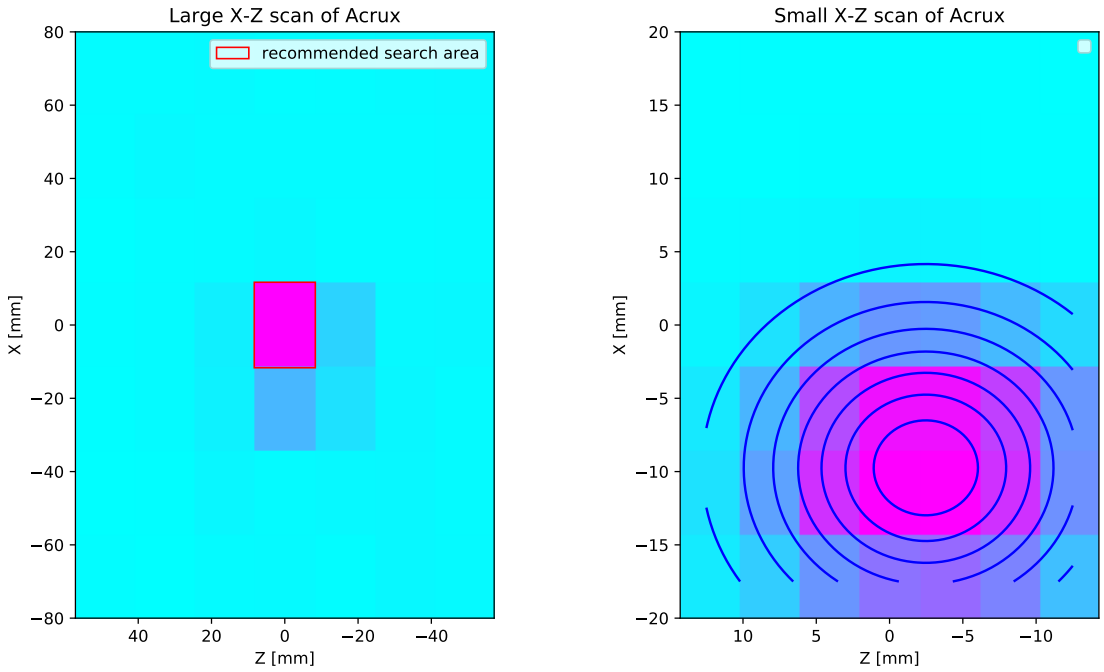

(a) The rough Z-X scan is performed and plotted as a heatmap. A rectangle is drawn around the brightest pixels. In the case of a rough scan oftentimes, this is only one pixel.

(b) The fine scan only scans the proximity of the rectangle from the rough scan. This allows for a better resolution. The blue lines show the contours of the gaussian that is fitted to the heatmap. The fit parameters can be found in table 4.3.

Figure 4.12: Run of an initial optimization, performed on the CT4 telescope during the campaign.

parameter	z_0 [mm]	x_0 [mm]	σ_z [mm]	σ_x [mm]	A [MHz]
value	-2.47 ± 0.10	-9.74 ± 0.09	7.51 ± 0.12	6.84 ± 0.12	391 ± 5

Table 4.3: Fit parameters of the gaussian fit as seen in fig. 4.12b. The equation of the fitted gaussian can be found in eq. (4.1).

The rates which were achieved through these optimizations (up to $800\,\mathrm{MHz}$ per PMT for bright objects such as Acrux), were at or above the previously calculated expected values.
One can therefore conclude, that the initial optimization worked quite well in general, even though the last part had to be done manually.

Continuous Optimization

The 2022 campaign was the first campaign of the AQO group at the H.E.S.S. telescopes. Hence, the group had no good approximation of the time intervals in which the rate would have to be optimized. Even though the pointing model of each telescope can be used to get a good estimation of the misspointing in altitude and azimuth, this only gives a rough estimate of the system's performance over time, as the stability of the optical system under a change of the misspointing was not known. Another issue was that automatic pointing corrections would need to be coordinated between the two telescopes, which was not feasible given the used software at the time. Therefore, the continuous optimization was performed manually by the operators. The following strategy was used:

1. Wait until the rate (measured live by the workstation) drops by more than $20\,\%$.
2. Vary Mirror Z around the initial value and find the maximum.
3. Vary Camera X around the initial value and find the maximum.
4. Vary Camera Z around the initial value and find the maximum.
5. Vary Mirror Y around the initial value and find the maximum.
6. Go back to 1.

This strategy proved to be quite efficient. Using this strategy, some observations were made:

- Normally an adjustment of Mirror Y is not necessary and only has minor impact on the rate. However, if Camera Z runs into its physical limit (respectively cannot move where it would be optimal), this parameter can help to lessen that problem.
- All these optimizations are only one-dimensional. Hence, they could easily be automated. Still, this was not implemented during the campaign, as the function of the software was of utmost importance and there was no time for long debugging-sessions.
- The time interval between two cycles of optimizations reached from $10\,\mathrm{min}$ to $30\,\mathrm{min}$. While the misspointing and therefore the rate proved to be more stable close to zenith, leading to longer times between the cycles of optimization, observations closer to the horizon required more frequent readjustments.

Overall the campaign team came to the conclusion that the rate optimization worked quite well, even though further automation would be favorable, especially when thinking about establishing a permanent intensity interferometry setup at H.E.S.S. that should be as easy to use as possible.

4.3.3 X-Y Measurement with Variable Z on the Telescope

In addition to the regular star-observations, which were the main aim of the campaign, the X-Y measurement with variable Z (compare section 4.1.3) was tested on closer examining the light beam of CT4. To get high rates and a low background, the telescope was pointed at Acrux for these measurements. This meant that at the time of the measurement (between 21:00 and 22:00 on April 20$^{\text{th}}$ 2022), the telescope was pointing at Alt: $\approx 46°$ and Az: $\approx 164°$. As there was not as much time as for the lab measurement in this mode ($3\,\mathrm{h}$ compare section 4.1.3), only 4 X-Y scans of lower resolution were performed, which took $\approx 45\,\mathrm{min}$.
The recorded heatmaps are shown in fig. 4.13 to fig. 4.16. The found fit parameters for the Gaussians are displayed in table 4.4. Note that ΔZ is increasing as the camera moves towards the mirror. It is set to 0 for the optimal position, as determined by the initial optimization procedure, which was used during the campaign. Additionally, Mirror Phi and Mirror Psi were set to 0.

ΔZ [mm]	x_0 [mm]	y_0 [mm]
-34.2	9.30 ± 0.51	0.44 ± 0.21
-17.7	8.19 ± 0.25	-1.54 ± 0.14
0.0	4.97 ± 0.09	-1.66 ± 0.10
15.3	6.29 ± 0.07	-4.25 ± 0.13

Table 4.4: Fit parameters of x_0 and x_0 of the individual X-Y scans. For an explanation of the parameters see eq. (4.1).

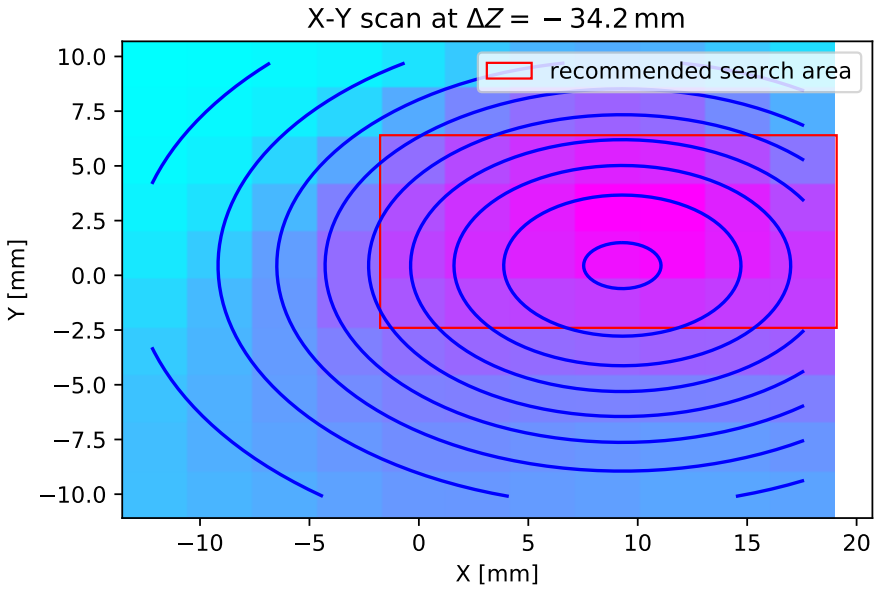

Figure 4.13: X-Y scan at $\Delta Z = -34.2\,\mathrm{mm}$

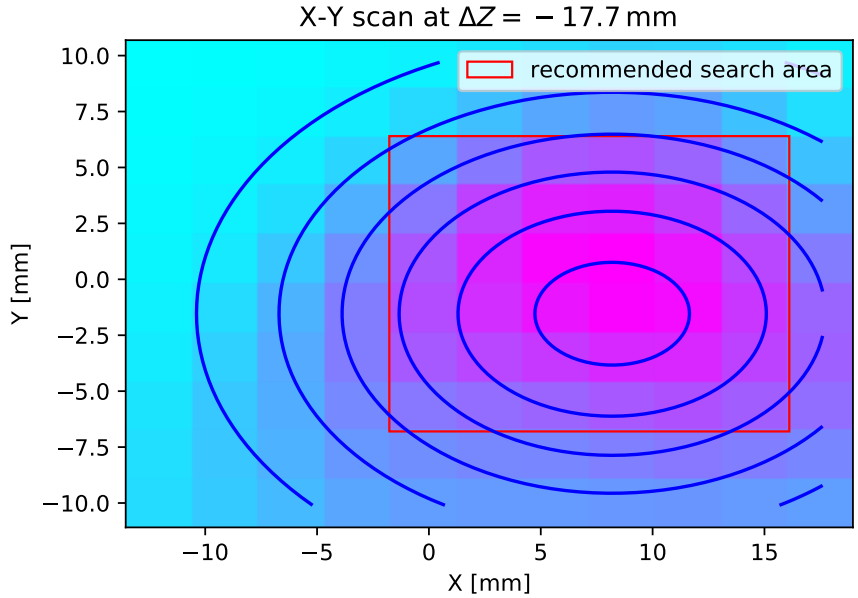

Figure 4.14: X-Y scan at $\Delta Z = -17.7\,\mathrm{mm}$

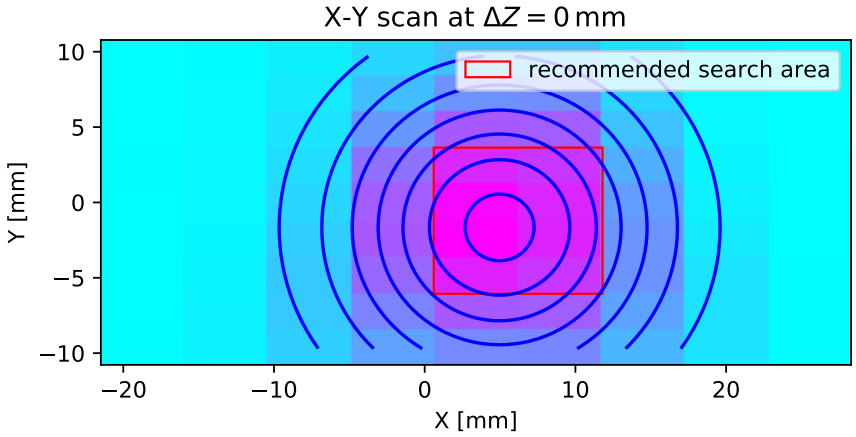

Figure 4.15: X-Y scan at $\Delta Z = 0\,\text{mm}$

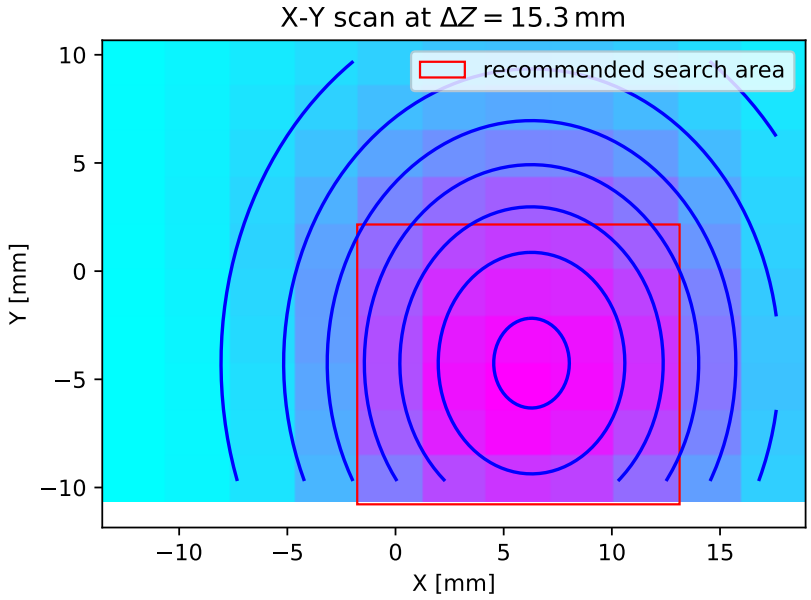

Figure 4.16: X-Y scan at $\Delta Z = 15.3\,\text{mm}$

Plotting the values of x_0 and y_0 over ΔZ, one can investigate whether the incoming light beam is perpendicular to the lid of the telescope. As explained before (compare section 4.1.3), a linear function ($x_0 = c \cdot \Delta Z + t$) is fitted to the data.

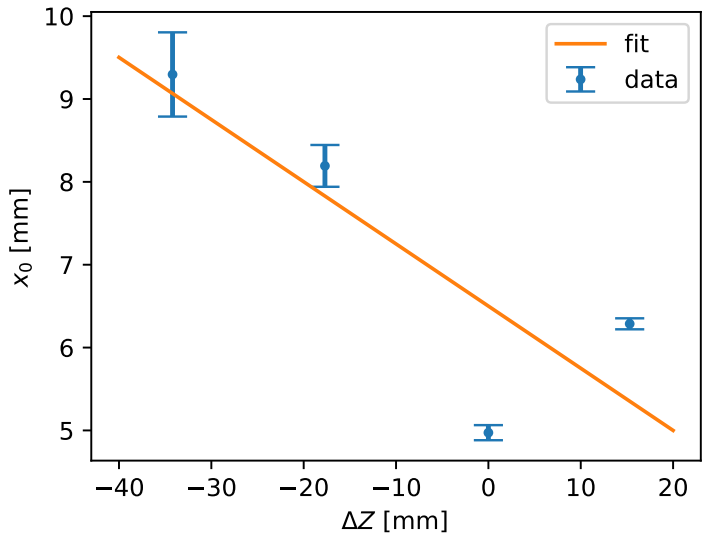

Figure 4.17: Plot of x_0 over ΔZ. In the optimal case (incoming light perpendicular to the lid), x_0 would stay constant as ΔZ changes. This is clearly not the case, as one can see in this figure (also compare fit parameters in section 4.3.3).

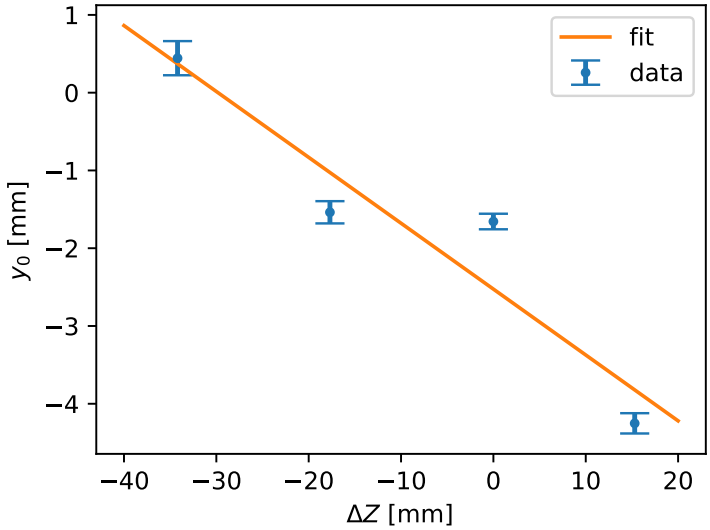

Figure 4.18: Plot of y_0 over ΔZ. In the optimal case (incoming light perpendicular to the lid), y_0 would stay constant as ΔZ changes. This is clearly not the case, as one can see in this figure (also compare fit parameters in section 4.3.3).

dataset	c	t [mm]	calculated angle of incidence γ [°]
x_0	-0.0750 ± 0.0350	6.50 ± 0.73	4.29 ± 2.00
y_0	-0.0847 ± 0.0004	-2.53 ± 0.19	4.84 ± 0.02

Table 4.5: Fit parameters and calculated angle of incidence (α) for a linear fit to the x_0 and y_0 values over ΔZ.

One can see in section 4.3.3, the slope of the fitted linear functions is non-zero. As done before (compare section 4.1.3), one can calculate the angle of incidence (γ) from the slope (compare section 4.3.3).

The angles γ_x and γ_y correspond to the angles α and β as defined in section 2.2.2. Even though the mechanical setup would be able to correct for α and β of up to 9°, one needs to check whether these values seem realistic, given the context.
If one assumes, that the light coming from the dish creates a cone around an imaginary central ray, this central ray can only hit the lid at an angle if the center of the telescope and the camera are not in line.
It is easy to calculate that an angle of incident $\alpha = \gamma_\mathrm{x} = (4.29 \pm 2.00)°$ (respectively $\beta = \gamma_\mathrm{y} = (4.84 \pm 0.02)°$) would translate to a vertical (resp. horizontal) movement of $\Delta X = d \cdot c = 15\,\mathrm{m} \cdot (-0.0750 \pm 0.0350) = (-1.13 \pm 0.53)\,\mathrm{m}$ (resp. $\Delta Y = d \cdot c = 15\,\mathrm{m} \cdot (-0.0847 \pm 0.0004) = (-1.271 \pm 0.006)\,\mathrm{m}$). These values are obviously not realistic, as the telescopes were not flexed by that order of magnitude during the measurements. Most likely the bad performance of this method is due to the change in pointing over time, as the telescope moves. Of course this effect was not seen in the lab, as a time stable setup was used there.

It is therefore reasonable to assume that an X-Y measurement with variable Z is not able to provide the desired information about the telescope's light cone. Hence, such a measurement is not desirable during productive operations of the telescope.

4.3.4 Performance and Possible Improvements of the Used Software

In the last two sections, the performance of the software under real conditions on the H.E.S.S. telescopes were examined. Generally, the campaign team which operated the intensity interferometry setup during the whole campaign, was satisfied with the way the optimization worked and operations were never prohibited by insufficient pointing corrections. Even though optimization routine worked well, as discussed in section 4.3.2, further improvements could be made to both the initial and the continuous optimization routine:

- The initial optimization routine should be completed by re-implementing the Camera Z step. This would fully automate the initial optimization, getting it closer to automatic

operation. It might also be advisable to fit the datapoints of this measurement with a more appropriate function, to save time by taking less individual datapoints.

- It was shown, that the X-Y mode with variable Z is not helpful at the telescope. As the used optimization routine delivered satisfactory results, it has proven to be a reasonable approach.
- The continuous optimization, as done by hand, was efficient and led to stable rates. Therefore, the simple algorithm that was used, should also be implemented to work automatically.
- Further adjustments, also to other parts of the AQO group's software, need to be made, to allow for fully automatic pointing corrections, as the control and coordination of them needs to be done centrally.

Chapter V

Conclusion and Outlook

This work examined the optimization of photon flux in the intensity interferometry setup of the AQO group at ECAP. In the beginning, the mechanical, optical and electrical setup were introduced and explained. Additionally, the H.E.S.S. phase I telescopes were described with respect to their behavior during measurements for intensity interferometry.
Afterwards, the used software was explained, as well as the various measurement modes which were implemented by the author. This was followed by extensive testing of the used software in the lab, which lead to a formulation and implementation of an automated optimization routine.

The experiences from the lab were then taken to the H.E.S.S. site in Namibia, where they were tested on the telescope. The initial optimization worked reliably, confirming the experience from the lab. A robust and precise routine for continuous optimization was developed and tested. Even though this worked quite well, the nature of the campaign did not allow for instant implementation of an automated continuous optimization routine.

Examinations of a complex optimization routine, that appeared promising in the lab, showed that such measurements are not advisable at the telescope. They take too much time and their results do not offer the quality needed for corrections. In contrast, it was shown that simple step by step optimizations of individual parameters are robust and more efficient, when adding reasonable constrains to them.

Even though the AQO group now has a working setup and semi-automatic optimization routine for the spot finding, there are interesting challenges ahead. After some more engineering heavy tasks and practice for operations, the next campaign at the H.E.S.S. telescopes is planned for fall 2022. And by its start, the data processing from the first campaign will have finished, hopefully leading to some great findings in the data.

As formulated in the first chapter, scientists have always been working on even better methods of measurement. Even though the AQO group at ECAP did not surpass the limits in the angular resolution of other telescopes (yet), its work lays ground for a next generation of intensity interferometers. Together with the other groups from MAGIC and VERITAS, they are steadily improving the quality of their observations. Intensity interferometry is therefore sure to have a bright future with the next generation of IACTs, namely the CTA telescopes.

List of Figures

List of Tables

Bibliography

[1] Wolfgang Demtröder. *Experimentalphysik 4*. Springer Spektrum, 2014.

[2] David R. Williams. Sun fact sheet. https://nssdc.gsfc.nasa.gov/planetary/factsheet/sunfact.html, 2018. [Online; accessed 2022-07-17].

[3] David R. Williams. Moon fact sheet. https://nssdc.gsfc.nasa.gov/planetary/factsheet/moonfact.html, 2021. [Online; accessed 2022-07-17].

[4] David R. Williams. Jupiter fact sheet. https://nssdc.gsfc.nasa.gov/planetary/factsheet/jupiterfact.html, 2021. [Online; accessed 2022-07-17].

[5] Mark Fox. *Quantum Optics - An Introduction*. OUP Oxford, New York, London, 2006.

[6] Mount Wilson Institute. Discovering mount wilson chapter 11: The stellar interferometer. https://www.mtwilson.edu/news/discovering-mount-wilson-chapter-11-the-stellar-interferometer/. [Online; accessed 2022-05-31].

[7] Michael D. Johnson, Katherine L. Bouman, Lindy Blackburn, Andrew A. Chael, Julian Rosen, Hotaka Shiokawa, Freek Roelofs, Kazunori Akiyama, Vincent L. Fish, and Sheperd S. Doeleman. Dynamical imaging with interferometry. *The Astrophysical Journal*, 850(2):172, nov 2017.

[8] R. Hanbury Brown, J. Davis, and L. R. Allen. The Angular Diameters of 32 Stars. *Monthly Notices of the Royal Astronomical Society*, 167(1):121–136, 04 1974.

[9] John Davis. Forty years of progress in long-baseline optical interferometry: 2005 robert ellery lecture. *Publications of the Astronomical Society of Australia*, 23:94–104, 2006.

[10] Leonard Mandel and Emil Wolf. *Optical Coherence and Quantum Optics*. Cambridge University Press, 1995.

[11] Dilleys Ferreira, Romain Bachelard, William Guerin, Robin Kaiser, and Mathilde Fouché. Connecting field and intensity correlations: The siegert relation and how to test it. *American Journal of Physics*, 88(10):831–837, 2020.

[12] H.E.S.S. Collaboration. High energy stereoscopic system - about h.e.s.s. Online, accessed 2022-06-08, https://www.mpi-hd.mpg.de/hfm/HESS/pages/about/.

[13] K BERNLOHR. The optical system of the h.e.s.s. imaging atmospheric cherenkov telescopes. part i: layout and components of the system. *Astroparticle Physics*, 20(2):111–128, nov 2003.

[14] R. Cornils, S. Gillessen, I. Jung, W. Hofmann, M. Beilicke, K. Bernlöhr, O. Carrol, S. Elfahem, G. Heinzelmann, G. Hermann, D. Horns, R. Kankanyan, A. Katona, H. Krawczynski, M. Panter, S. Rayner, G. Rowell, M. Tluczykont, and R. van Staa. The optical system of the h.e.s.s. imaging atmospheric cherenkov telescopes. part II: mirror alignment and point spread function. *Astroparticle Physics*, 20(2):129–143, nov 2003.

[15] Sebastian Konrad. Ray tracing simulation for astro quantum optics. Master's thesis, Friedrich-Alexander-Universität Erlangen-Nürnberg, 2021.

[16] LukeSkywalker92. Python tmcl client library. Online, accessed 2022-06-08, `https://github.com/LukeSkywalker92/pyTMCL`, 2018.

Thanks

Last but not least I want to thank everyone who supported me during the writing of this thesis. Special thanks goes to

Stefan Funk for trusting in me and my skills, advising me in my choices and sending me to Namibia.

Andreas Zmija for his open ears, his perspectives on my work and for working together on a par with each other.

Ashkhen Aristakessian for planting the seed that grew into a career as a physicist.

Naomi Vogel for being the best travel planner.

Tim Unbehaun for being a good companion through my whole time at FAU.

Tina, Matei and Rajshree for the community in our office and the good time we shared.

The H.E.S.S. local crew for getting us out of every mess we got ourself into (sometimes quite literally) and the Braais, which one cannot enjoy any better than with you guys.

All who read this thesis before submission for saving me from many large and small mistakes.

My parents for sponsoring me this whole time and helping me wherever needed. I would not have ever been able to get where I am now without you.

Erklärung

Hiermit bestätige ich, dass ich diese Arbeit selbstständig und nur unter Verwendung der angegebenen Hilfsmittel angefertigt habe.
I hereby certify that this thesis has been composed by me and is based on my own work, unless stated otherwise.

Erlangen den 22. Juli 2022

Frederik Wohlleben